CDF/ANAL/EXOTIC/CDFR/9472
Draft 2.0
18th August 2008

Search for Gluino-Mediated Sbottom Production in the MET+b-jet Sample

Miguel Vidal, Oscar González

CIEMAT, E-28040, Madrid, Spain

Abstract

Using data collected with the CDF detector in the Run II of the Tevatron, we analyzed events containing two or more jets and missing transverse energy searching for the presence of physics beyond the Standard Model. Two categories were made by requiring only one of the jets or at least two jets to be tagged as originating from a heavy-flavour quark in order to enhance the sensitivity to final states containing b-quarks. The analysis was optimized via two Neural Networks to search for the supersymmetric partner of the bottom quark produced from gluino decays. Results were obtained with 2.5 fb^{-1} of data and constrain the cross section production to be less than 50 fb at 95 % C.L.

Contents

1 Introduction **1**

2 Theoretical Motivation **1**

3 Dataset **6**

4 Monte Carlo Samples **7**
4.1 Signal Monte Carlo Samples 7
4.2 Background Monte Carlo Samples 7

5 The MET45 trigger efficiency **9**
5.1 The L1_MET25 trigger 9
5.2 The trigger at Level 2 10
5.3 The L3_MET45 trigger 11

6 Analysis Strategy **16**
6.1 Pre-selection Cuts 16
6.2 QCD Control Region 16
6.3 Lepton Control Region 17
6.4 Pre-optimization Control Region 17

7 Control Regions Results **18**

8 Signal Optimization **38**
8.1 Neural Network Architecture 38
8.1.1 QCD Multijets Neural Networks 39
8.1.2 Top pair Neural Networks 42
8.2 QCD Multijets Neural Network Results 44
8.3 Top pair Neural Network Results 47

9 Systematic Uncertainties **49**
9.1 Background Uncertainties 49
9.2 Signal Uncertainties 50

10 Results **53**
10.1 Signal Regions Results 53
10.1.1 Signal Regions 54
10.2 Observed Limit 56

A Top pair NN dependence on the top quark mass **59**

B Dependences of the MUTARE prediction (2 inclusive tags) with the first or second tagged jet **60**

References **67**

Acknowledgments **67**

1 Introduction

In the present analysis we search for sbottom quarks ($\tilde{b}$) produced though gluino ($\tilde{g}$) decays. We look for gluino pair production $p\bar{p} \rightarrow \tilde{g}\tilde{g}$, where the gluino decays to $\tilde{g} \rightarrow b\tilde{b}$ with the subsequent sbottom decay to a b-quark and the lightest neutralino ($\tilde{\chi}^0$), $\tilde{b} \rightarrow b\tilde{\chi}^0$. The neutralino is taken to be the Lightest Supersymetric particle (LSP) and R-parity conservation is assumed. Therefore, the gluino signature is 4 b-jets and large missing transverse energy ($\not{E}_T$).

For this analysis we use the inclusive $\not{E}_T$ trigger MET45. We define two control regions, one pre-optimization region and two signal regions. In the two control regions predicted distributions are compare with those measured in data using single and double tagged events (using the SecVtx tagging algorithm). We then perform a signal optimization by using two Neural Networks (NN) in order to reduce the two main backgrounds, the heavy-flavour QCD multi-jet production and the top pair production. Finally we perform a counting experiment comparing the number of observed events with the number of expected backgrounds events.

Previous results were obtained with 156 pb^{-1} [1] and 1.8 fb^{-1} [2] of Run-II data.

2 Theoretical Motivation

In the Minimal Supersymetric extension of the Standard Model (MSSM), to every fermionic Standard Model (SM) particle a bosonic superpartner is assigned and vice versa. Therefore, the SM quark helicity states q_L and q_R have scalar MSSM super-partners, which are also the mass eigenstates (in good approximation) for the first two generations. However, for the third generation, strong mixing can appear depending on the parameters of theory: tanβ (the ratio of the VEV's of the two Higgs fields) and A$_b$ (the Higgs-sbottom trilinear coupling). The masses of the $\tilde{b}$ are given by:

$$m_{\tilde{b}^2_{1,2}} = \frac{1}{2}[m^2_{\tilde{b}_L} + m^2_{\tilde{b}_R} \pm \sqrt{(m^2_{\tilde{b}_L} - m^2_{\tilde{b}_R})^2 + 4m^2_b(A_b - \mu tan\beta)^2}]$$

If the tanβ is large, then there can be a large mass splitting in the sbottom sector, yielding $\tilde{b}$ masses in the reach of the Tevatron center of mass energies. Assuming R-parity conservation, SUSY particles are pair produced and the LPS must be stable. If in addition it is colorless and neutral, then it will escape from the detector undetected yielding large $\not{E}_T$.

The gluino pair production cross section is large compared to direct sbottom pair production of similar mass. At the Tevatron energies, gluinos are produced mainly through

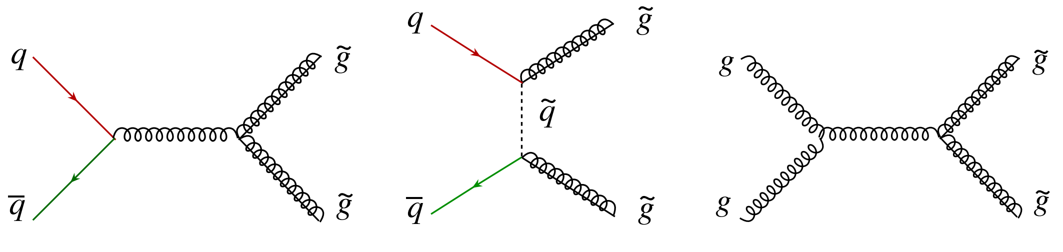

Figure 1: Leading Order gluino pair production mechanisms at the Tevatron center of mass energies.

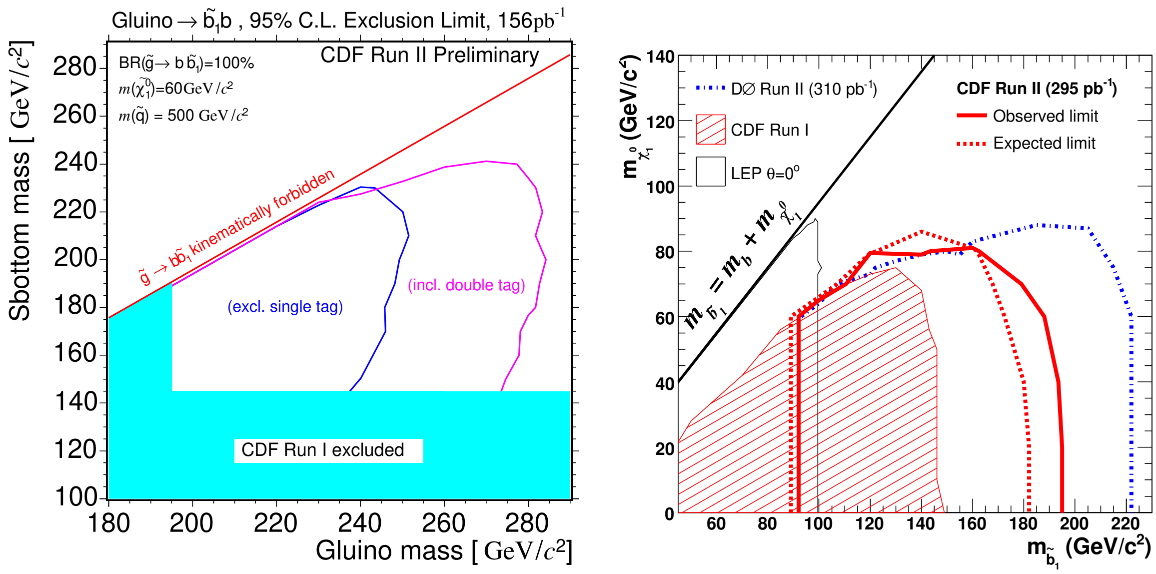

Figure 2: Previous CDF result with 156 pb^{-1} (on the left) and results for the sbottom direct production (on the right).

quark-antiquark annihilation and gluon fusion Figure 1, with the former dominating for high x. If the sbottom is light enough, then the two body decay $\tilde{g} \to b\tilde{b}$ would be kinematically allowed.

In our region of interest ($m_t, m_{\tilde{\chi}^+} > m_{\tilde{b}} > m_{\tilde{\chi}^0}$) the dominant decay channel is sbottom into bottom quark and neutralino $\tilde{b} \to b\tilde{\chi}^0$, with no other available decays channels since we require $m_{\tilde{b}} < m_t, m^{+}_{\tilde{\chi}}$. Hence, we assume a Branching Ratio of 100% for the $\tilde{b} \to b\tilde{\chi}^0$ decay.

One can also think of a scenario where the second neutralino $\tilde{\chi}^0_2$ is lighter than the sbottom quark. In this case $\tilde{b} \to b\tilde{\chi}^0_2$, with the second lightest neutralino decaying into leptons and LPS ($\tilde{\chi}^0_2 \to ll\tilde{\chi}^0_1$). Such a signature could be observed by multileptons search and is not considered here.

Figure 2 shows the previous limits on the direct and gluino-mediated sbottom production at Tevatron.

In order to get the predictions for our signal, we used the program PROSPINO [3] to compute the total production cross section and PYTHIA [4] to estimate the event acceptance in the detector and in the application of our selection cuts.

For the NLO cross sections of gluino pairs, the calculation does not depend on the sbottom mass or the neutralino mass. However, there is a dependence on the mass of the first squarks due to their presence in the diagrams. The main dominant contribution is coming from those squarks associated to the lightest quarks, specifically $\tilde{u}$ and $\tilde{d}$ due to their presence as valence quarks in the proton and antiproton. In Fig. 3 we show the cross section of gluino-pair production for $m(\tilde{g}) = 250$ GeV$/c^2$ and $m(\tilde{g}) = 350$ GeV$/c^2$ as a function of the squark masses[1]. We observe a strong dependence for the Leading-order and Next-to-leading cross sections on the mass of the squarks.

Due to this dependence the analysis needs to be performed with a clear assumption on

[1] As this is done in PROSPINO, the masses of the squarks associated to the light quarks are degenerated, and we always assume that.

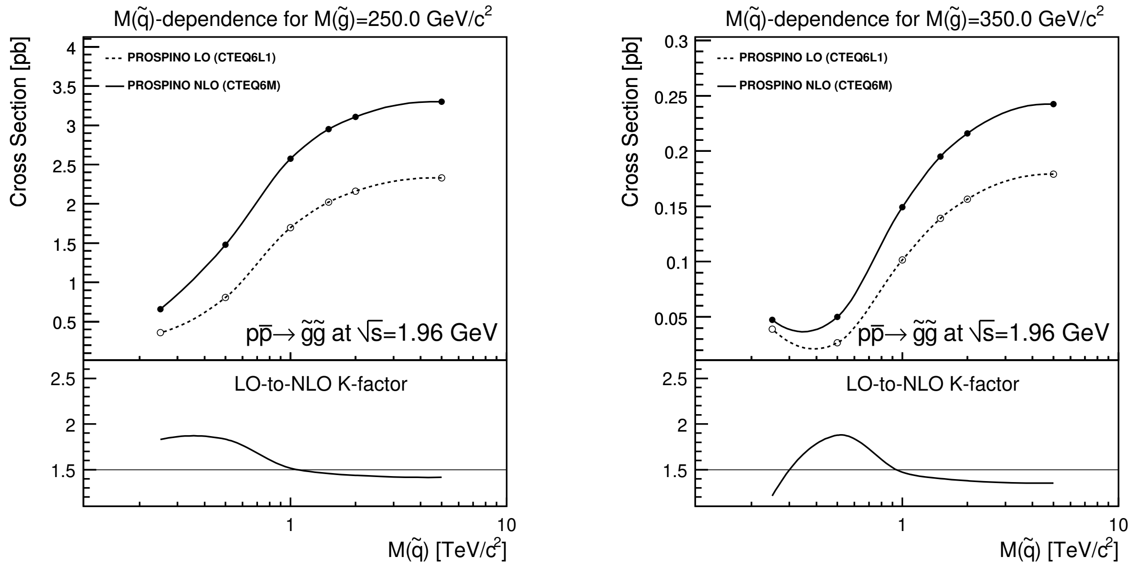

Figure 3: LO and NLO cross section of gluino-pair production at the Tevatron Run II as predicted by PROSPINO as a function of the mass of the squarks of the first two families. The predictions are shown for values of the gluino mass of 250 GeV/c^2 (left) and 350 GeV/c^2 (right).

the mass of the squarks. We decided to use the value of 500 GeV/c^2 as it was done in the previous analysis [1]. This value leads to a conservative estimate of the cross section since the larger the mass of the squark, the larger the cross section. Using a value much smaller than 500 GeV/c^2 may break the assumption that the decay of the gluino is dominated by $\tilde{g} \to b\tilde{b}_1$.

Under this assumption, we compute the cross section of the gluino-pair production process for the range of masses we are interested in. This is shown in Fig. 4 using the CTEQ6M set of Parton Distribution Functions [5]. The cross section falls very rapidly when increasing the mass of the gluino, but the absolute values are reasonable for the analysis to reach unexcluded regions of the parameter space.

As a comparison, in Fig. 5 we show the equivalent cross section for sbottom-pair production. It should be noticed that for similar masses of the gluino and sbottom, the production of gluino has a much larger cross section, leading to the fact that even for smaller mass of the sbottom, the channel we are considering here provides larger sensitivity than the direct search of sbottom-pair production due to a larger cross section and a signature that is much cleaner than that of the sbottom-pair production.

It should be noticed that since we plan to quote a limit on the production cross section, we assume that number has not uncertainty. The predicted cross section has uncertainties, as shown in the plot, but they do not affect the result of the analysis. For this reason, the central cross sections predicted by PROSPINO are considered as exact inputs of the models when necessary. For this reason, we list some reference numbers of the computed cross sections that we are using in the analysis in the following table:

Gluino Mass [GeV/c^2]	225	250	275	300	325	350	375	400
NLO Cross section [pb]	3.50	1.48	0.635	0.273	0.117	0.0499	0.0210	0.00872

As indicated above, we have also used PYTHIA to generate actual events for our signal

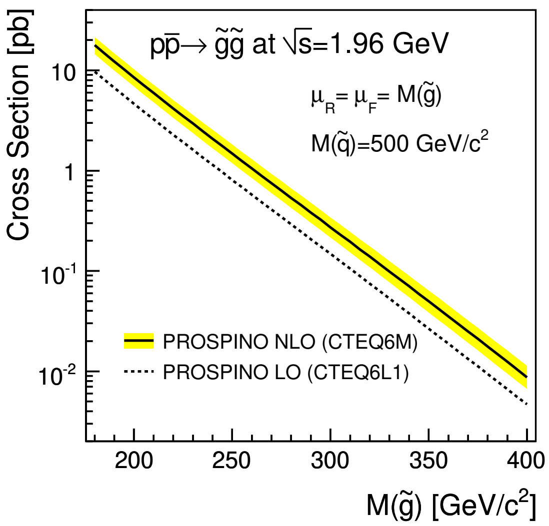

Figure 4: LO and NLO cross sections of gluino-pair production at the Tevatron Run II as predicted by PROSPINO as a function of the gluino mass. A mass of 500 GeV/c^2 has been assumed for the squarks of the first two families.

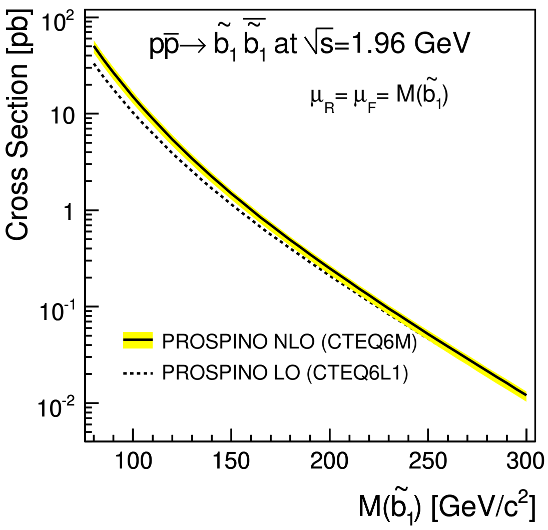

Figure 5: LO and NLO cross sections of direct sbottom-pair production at the Tevatron Run II as predicted by PROSPINO as a function of the lightest sbottom mass.

that are passed through the detector simulation and used to estimate the acceptance for different regions in the parameter space. We have produced these events by setting all the SUSY parameters by hand in PYTHIA, including the corresponding decay chain and the assumed branching ratios.

The main variables affecting the PYTHIA generation are the masses of the actually produced particles (gluino, sbottom and neutralino) that are set accordingly for the different points. Our main samples are those having $m(\tilde{\chi}_1) = 60$ GeV/c^2, but we also generated some samples having $m(\tilde{\chi}_1) = 100$ GeV/c^2 for future use.

The samples were generated using the official CDF MC tarball, the one identified as *6.1.4mc_g (stripped)*. We setup our private tcl that are specific for the gluino-pair production but kept all the parameters and configuration to their standard (i.e. the most commonly used) values. We therefore generated events using the *Minimum-Bias Overlay* option and used the run-dependent configuration. Each sample contains between 95 and 150 thousand events, which is far more than enough for our purposes.

We have studied the dependence of the acceptance with the mass of the squark using samples that were generated with different values of that parameter. It should be remarked that we assumed that the masses of the squarks of the first two families are degenerated. The result of this study is shown in Fig. 6 where we observe that such a dependence is really marginal. This imply that the analysis may be performed independently of the assumed mass of the squarks. However, due to the large dependence of the gluino-pair production cross section on this parameter, the interpretation of the final result can only be done with the assumption of a specific value of that mass, being that 500 GeV/c^2, as motivated above.

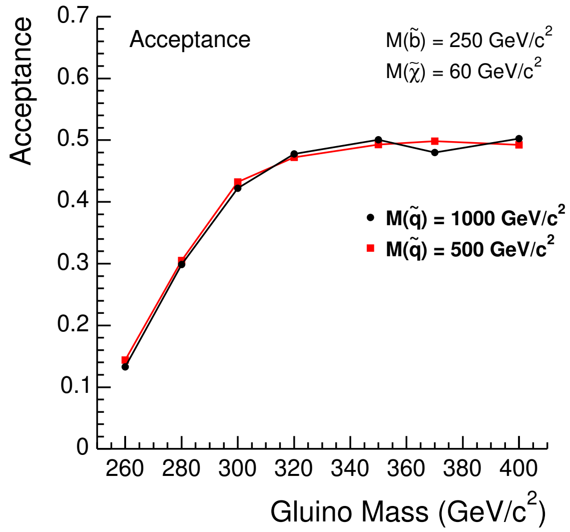

Figure 6: Acceptance efficiency as a function of the gluino mass for two different assumptions of the squark mass for fixed values of the other parameters.

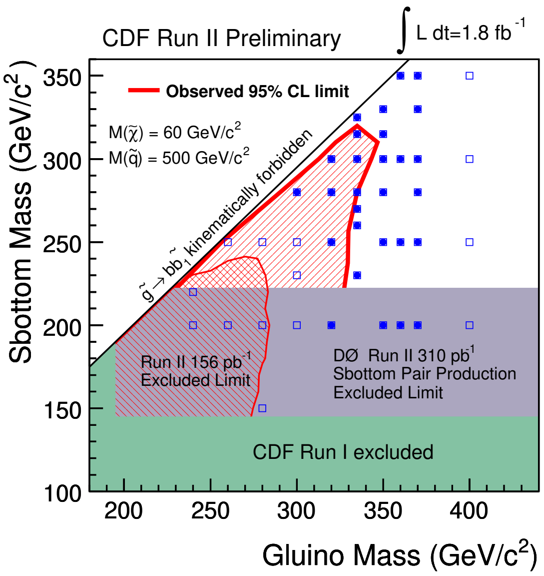

Figure 7: PYTHIA Generated samples (blue squares) for the gluino-pair production process in the parameter plane of the mass of the gluino and the mass of the sbottom. Previous (1.8 fb^{-1}) 95% C.L. exclusion limits are also shown.

A plot showing the generated samples in the context of the previous limits is shown in Fig. 7. We have tried to give a good coverage of the interesting region, although we do not know a priori the location of the final limit. We will interpolate the numbers when needed.

3 Dataset

The analysis presented on this note is based on Run II data collected between March 2003 and April 2008. This period of time corresponds to the run number range 141544-261005. The DQM GoodRun List v23 was used.

The data were collected with the three-level logic trigger MET45. A sequence of cuts on the $\not\!\!E_T$ is required at each level. At Level 1 it requires $\not\!\!E_T$ above 25 GeV, at Level 2 it requires $\not\!\!E_T$ above 35 GeV and at Level 3 it requires $\not\!\!E_T$ above 45 GeV.

Due to a problem in the implementation of the cut at Level 2 during a period of time the cut on the Level 2 was above $35 \times \sqrt{8}$ GeV. For this reason we are removing for this analysis the run number range 178637-192363 where this problem was present.

We remove also for this analysis the run number range 217990-220272 and 245448-246231 due to a hot tower in the calorimeter [6].

A hardware problem present at Level 1 in the trigger makes that several events are missing from the high-$\not\!\!E_T$ region, due to saturation in the tower energy (at 127.5 GeV). We recover this events by using the method described in reference [7]. We estimate the amount of data recovered with this method as an 4% of the total data sample computed in the basic selection region after the cuts listed below. The effect of this problem on the trigger efficiency at Level 1 is described later in this note in section 5.

The final luminosity, taking in account the previous aspects, used in the present analysis is 2.52 fb^{-1}.

All the events from this dataset used in the analysis have passed some basic requirements:

- Goodrun list v23
- At least one vertex with Q $\geq$ 12
- $|Z_{vtx}| \leq$ 60 cm
- At least two jets with corrected transverse energy, $E_{T,j} \geq$ 25 GeV
- At least one jet with $E_{T,j} \geq$ 35 GeV
- At least one central jet, $|\eta_{jet}| \leq$ 0.9
- Corrected MET above 70 GeV
- Standard clean-up cuts for MET analysis [8]

4 Monte Carlo Samples

The present section showns the Monte Carlo samples used in this analysis, all of them generated with PYTHIA. Some of the samples used for the background estimation are generated in a private way but are public for the rest of the collaboration. In particular the QCD sample, with a huge number of events, is available in the QCD group.

4.1 Signal Monte Carlo Samples

Signal Monte Carlo samples were generated with PYTHIA in order to cover the phase space under study as a function of the sbottom mass and gluino mass. The gluino mass was varied between 240 GeV/c^2 to 400 GeV/c^2 and the sbottom masses from 150 GeV/c^2 to 350 GeV/c^2. The neutralino mass was fixed to 60 GeV/c^2, while the squark mass was fixed to 500 GeV/c^2. The points generated are showed in the Fig. 8 with the previous limit obtained for the previous version [2] of the present analysis, the excluded region by the sbottom pair production analysis made by DØ [9] and the region excluded by CDF Run I.

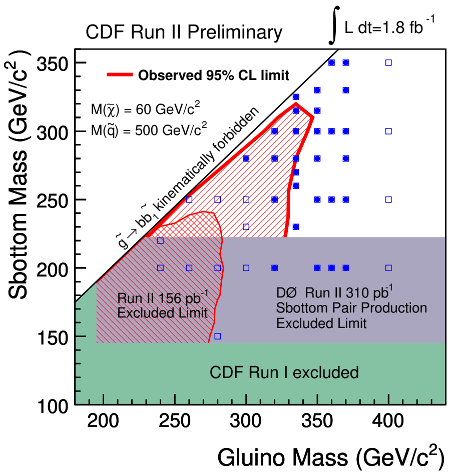

Figure 8: SUSY points in blue generated with PYTHIA.

4.2 Background Monte Carlo Samples

The SM background in this analysis is dominated by $t\bar{t}$ events and mistags. In addiction, there are contributions from Z and W production in association with jets, single top and diboson production. A detailed description of all the Monte Carlo samples used in the analysis are in Table 1. This Table 1 lists the official name, source, cross section, number of generated events, luminosity, K-factor and Willis' factor for each sample. The Willis' factor is a correction, usually applied in data, to manage the fact that in analysis we don't use events with $|Z_{vtx}| > 60$ cm but the luminosity detector computes them. This correction apply also in the Monte Carlo but it is slightly different that the data factor.

The QCD sample listed in Table 1 is used for checking and optimization purposes since the QCD background for the present analysis is obtained from data as it is described in note [10].

Table 1: List of Monte Carlo PYTHIA samples used for the background estimation.

Process	Official name	Source	Cross section (units)	N events	Luminosity (fb^{-1})	K-factor (used)	Willis' factor
Incl. QCD ($p_T > 40$)	q8ib01_...	private	1.33 (μb) (LO)	72,738,179	0.0546 (LO)	(norm)	0.967
$t\bar{t}$ (m=171.5)	ytop71	Top WG	7.3 $\pm$ 0.8 (pb)	945,906	129.6	n/a	0.963
Single-top (t)	w8ib01_...	private	1.98 $\pm$ 0.25 (pb)	413,225	208.7	1.0	0.960
Single-top (s)	w8ib01_...	private	0.88 $\pm$ 0.11 (pb)	351,293	399.2	1.0	0.961
$W \to e\nu$	wewkge	EWK WG	1960 (pb)	12,964,244	6.614 (LO)	1.4	0.964
$W \to \mu\nu$	wewk8m	EWK WG	1960 (pb)	6,353,392	3.242 (LO)	1.4	0.964
$W \to \tau\nu$	wewkat	EWK WG	1960 (pb)	6,491,954	3.312 (LO)	1.4	0.964
$Z \to ee$	zewkad	EWK WG	355 $\pm$ 3 (pb) (LO)	6,491,954	18.29 (LO)	1.4	0.963
$Z \to \mu\mu$	zewk9m	EWK WG	355 $\pm$ 3 (pb) (LO)	6,499,954	18.31 (LO)	1.4	0.963
$Z \to \tau\tau$	zewkat	EWK WG	237.8 $\pm$ 3 (pb) (LO)	6,461,515	27.26 (LO)	1.4	0.964
$Z \to \nu\nu$	w8ib01_...	private	73.6 (pb) (LO)	10,737,014	135.87 (LO)	1.4	0.960
$Z \to bb/cc$	w8ib01_...	private	1.56 (nb) (LO)	32,988,444	21.15 (LO)	1.4	0.960
WW	wvik0w	private	12.4 $\pm$ 0.8 (pb)	478,038	38.55	n/a	0.963
WZ	wvik0z	private	3.64 $\pm$ 0.3 (pb)	520,259	142.9	n/a	0.964
ZZ	w8ib01_...	private	1.10 (pb) (LO)	1,497,740	1361.6 (LO)	1.4	0.961

5 The MET45 trigger efficiency

In this chapter we study the trigger efficiency for the analysis. Calculation is performed using data and it is intended to be applied to the Monte Carlo predictions for signal and backgrounds.

To estimate the efficiency in a region of interest, we start with a minimal selection that guarantees both efficient running and close selection to the events we need. This minimal selection is similar to the basic selection applied in the analysis:

- Good run list requiring good calorimetry and good silicon as in the analysis.
- Vertex, MET clean-up cuts (including central jet requirement) and jets corrected to Level 5.
- At least two jets with $E_T > 25$ GeV and $|\eta| \leqslant 2.4$, with at least one of them having $E_T > 35$ GeV.
- One of the jet has to be central, satisfying $|\eta| \leqslant 0.9$.
- $\not\!\!E_T > 15$ GeV.

The samples that are used for the efficiency calculation are described in the corresponding section. The trigger biases are dealt with accordingly.

5.1 The L1_MET25 trigger

At Level 1, the path under study requires that the $\not\!\!E_T$ is above 25 GeV. This quantity is computed using the Level 1 resolution. The parameterization is done with the offline corrected $\not\!\!E_T$, providing a long turn-on transition due to the poor resolution at Level 1.

In addition, hardware problems in the trigger makes that several events are missing from the high-$\not\!\!E_T$ region, due to saturation in the tower energy.

Results are shown in Fig. 9 for the kinematic selection indicated previously. We used the high-p_T muon sample (HIGH_PT_MUON) and the JET50 sample to select the events. Events from the JET20 sample are used to cross-check the result.
The observed efficiencies are parameterized with the following sigmoid function:

$$\epsilon(\not\!\!E_T) = \frac{a}{1 + \exp\left(-\frac{\not\!\!E_T - b}{c}\right)} \quad , \tag{1}$$

which gives a good representation of the upper part of the turn-on functions. The lower part is not that well reproduced but it will be ignored in the parameterization due to the large uncertainty of the efficiency in that region.

It should be remarked that the use of the events with low corrected $\not\!\!E_T$ that are able to pass the trigger selection is discouraged due to their pathological nature. In our analysis we always select events having a reasonably high $\not\!\!E_T$, mostly motivated for the trigger turn-on functions.

We observe that the different samples give a slightly different turn on. The most worrisome result is that the plateau does not reach a 100% efficiency as one would expect. This has been investigated and the explanation is a bug in the Level 1 reconstruction when

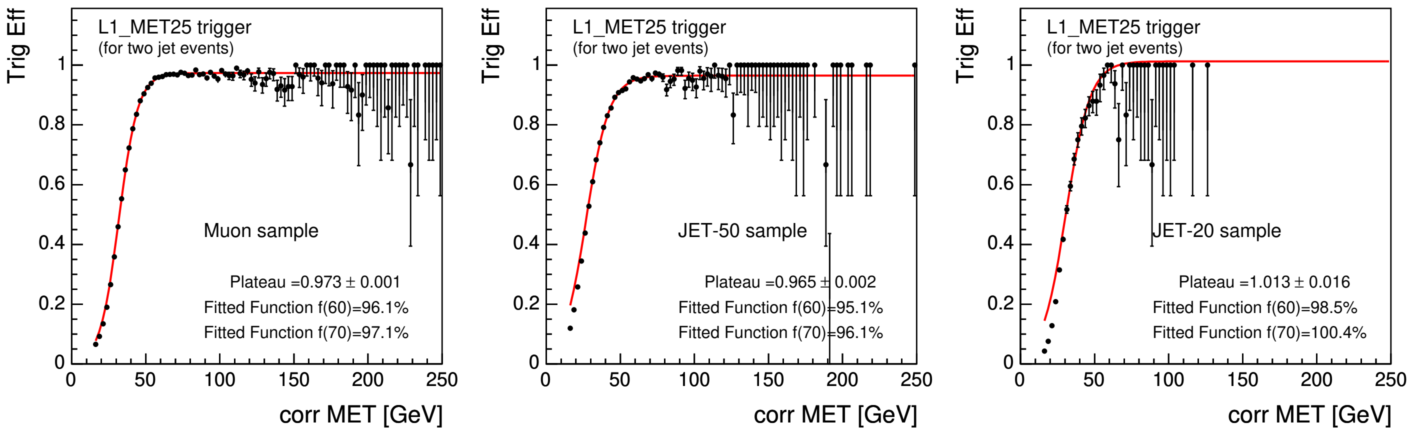

Figure 9: Turn-on of the L1_MET25 trigger for the 1.78 fb^{-1} sample as a function of the corrected $\not\!\!E_T$. Events are selected using the basic cuts on the HIGH_PT_MUON, JET50 and JET20 samples (from left to right).

there are saturated towers: for events containing saturated towers at L1, the $\not\!\!E_T$ may be miscalculated and should be saturated. However, it is not, giving rise to the bug and the inefficiency at high $\not\!\!E_T$.

In order to fix the problem of the missing events, we recover them by using the method described in reference [7] which consists on getting events passing the JET100 sample and not passing the cut at Level 1 for the $\not\!\!E_T$ triggers. Adding this requiriment as an alternative path collecting the events, we reconstruct the turn-on functions shown in Fig. 10.

The obtained functions show a clear 100% plateau that prevents to quote any uncertainty for very high $\not\!\!E_T$ values. However, we will have some uncertainty in the region close to the turn-on.

5.2 The trigger at Level 2

At Level 2 the MET45 trigger path has been modified to take into account the rise in the rate as the instataneous luminosity of the Tevatron increases. In the run period we are considering for the analysis the cut at Level 2 was always applied in the Level-1 reconstructed $\not\!\!E_T$. Three periods can be distinguish:

- An auto-accept Level-2 selection (i.e. $\not\!\!E_T(L1) \geqslant 25$ GeV).
- A problematic region where the cut was mistakenly set to a pretty large value.
- A selection based on $\not\!\!E_T(L1) \geqslant 35$ GeV.

As mentioned in the data sample description in section 3, we do not include the run period for which the Level 2 was not correctly implemented.

Since the data samples we are using to estimate the efficiency are exactly the same as the one we plan to use for the actual analysis and the fact that we are constrained to a region where the efficiency is high enough, we should be able to compute the averaged

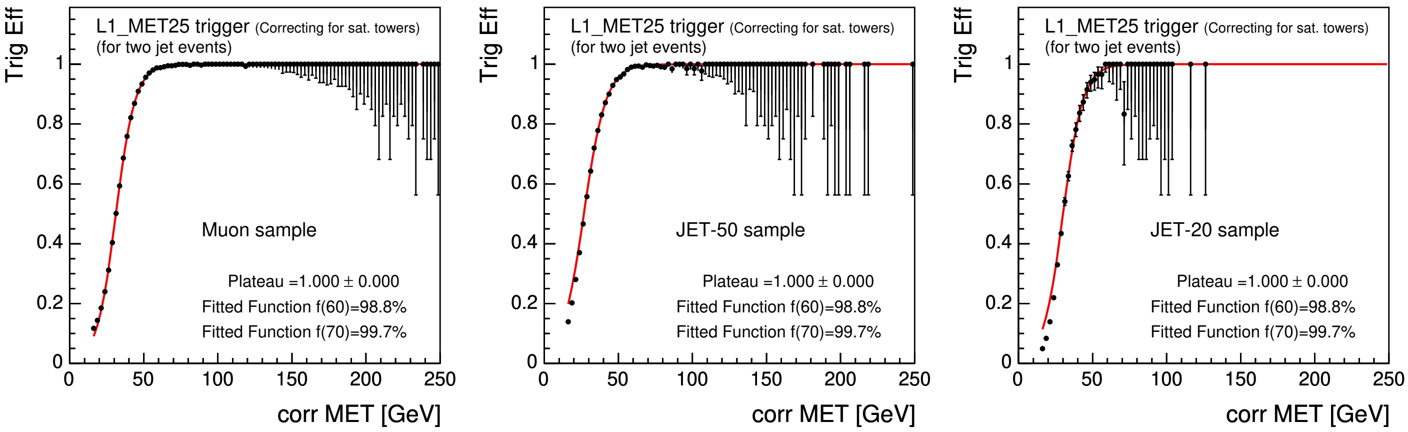

Figure 10: Turn-on of the L1_MET25 trigger for the 1.78 fb^{-1} sample as a function of the corrected $\not\!\!E_T$. Events are selected using the basic cuts on the HIGH_PT_MUON, JET50 and JET20 samples (from left to right) and the selection is taking into account the recovery of the events containing saturated towers and failing the L1_MET25 trigger.

efficiency on the datasample by applying the cut that was actually implemented for each particular run.

In addition, we compute the efficiency for events that satisfied the Level-1 requirements, to completely factorized the different turn-on functions.

Plots in Fig 11 show the obtained efficiencies and fitted turn-on functions (as before, using the parameterization given in Eq. 1) for the several samples that we are using in this study. It should be noted that for Level 2 (and Level 3 in the following section) we can make use of the so-called *MET Back-up* sample that selects a prescaled subsample of events that passed the Level-1 requirement.

The efficiencies in the plots have already been corrected for events failing the Level-1 due to the saturated towers using the JET100 requirements at Level 2. Due to this, the efficiency reaches 100% for high $\not\!\!E_T$.

5.3 The L3_MET45 trigger

At Level 3, a simple cut on the L3-reconstructed $\not\!\!E_T$ is applied. In this case a resolution closer to that offline is achieved, but still not enough to assure a completely sharp turn-on.

For events passing the Level 1 and Level 2 requirements, we obtain the turn-on function shown in Fig. 12 for events in the HIGH_PT_MUON, the JET50, the JET20 and the *MET Back-up* samples.

As before, we parametrized the trigger efficiency with a sigmoid function. It should be noted that, as described in reference [7], the events that passed the Level 2 of the JET100 trigger but not the one in the $\not\!\!E_T$ are required to pass a cut on $\not\!\!E_T(L3) \geqslant 35$. This is enough to guarantee that the problematic events containing saturated towers are included in the sample, provinding full efficiency for events with high $\not\!\!E_T$.

Using the parameterization of all the considered levels and samples, we compute the total efficiency of the path by multiplying the fitted functions at the different levels for each

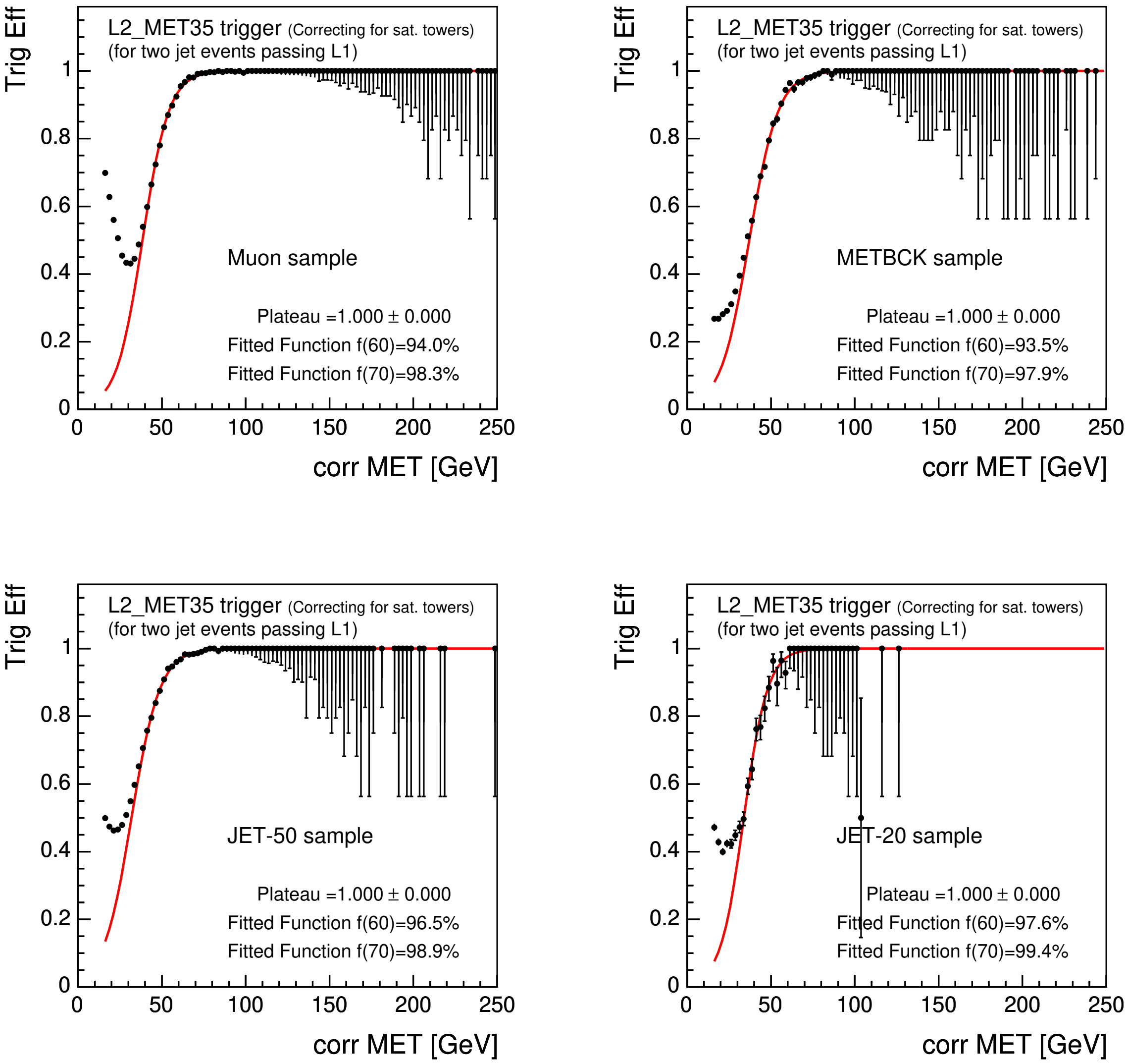

Figure 11: Turn-on of the Level-2 trigger for the 1.78 fb^{-1} MET45 sample as a function of the corrected $\not\!\!E_T$. Events are selected using the basic cuts on the HIGH_PT_MUON, *MET Back-up*, JET50 and JET20 samples (from left to right) and the selection is performed to take into account the recovery of the events containing saturated towers and failing the L1_MET25 trigger.

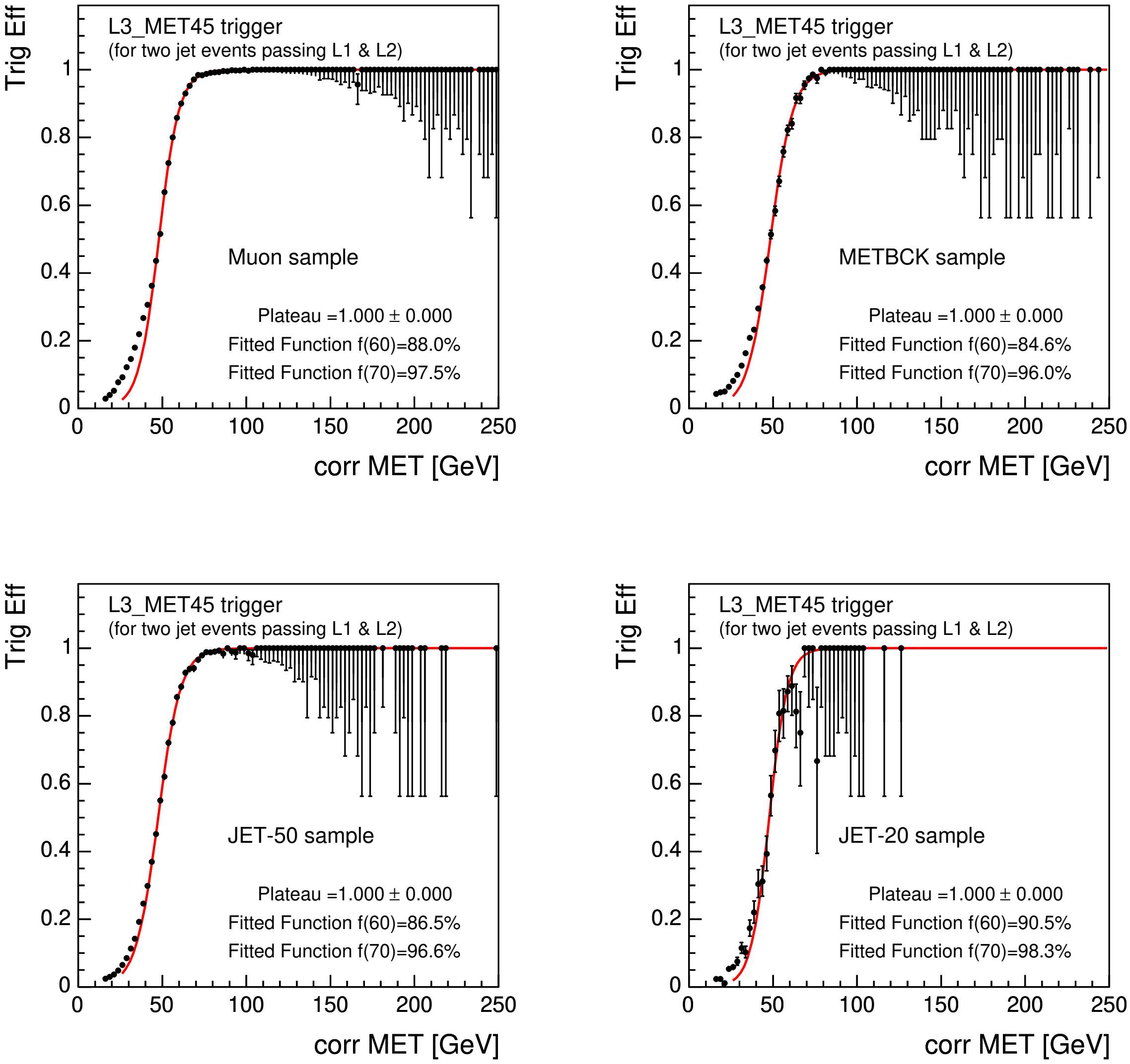

Figure 12: Trigger efficiency of the L3_ME435 requirement as a function of the corrected $\not\!\!E_T$ for events satisfying the basic selection cuts in the analysis and passing the requirements at Level 1 and Level 2.. Results are shown for the HIGH_PT_MUON, the *MET Back-up*, the JET50 and JET20 samples.

sample. We consider that the muon sample is the one closest to the selection of signal events contaning real $\not\!\!E_T$ and for this reason, it is taken as the central prediction for the efficiency.

The other predictions are used to estimate the uncertainty in the turn-on parameterization. It should be noted that the precision in the fit is larger than the differences among the results obtained by using the different samples. We quote the following uncertainty as a parameterization of the relative uncertainty.

$$\Delta\epsilon/\epsilon(\not\!\!E_T) = \begin{cases} 0.07 \cdot \left[\frac{90-\not\!\!E_T}{30}\right]^3 & \text{if } \not\!\!E_T < 90 \text{ GeV}, \\ 0.00 & \text{if } \not\!\!E_T \geqslant 90 \text{ GeV}. \end{cases}$$

Due to the big growing term, motivated by the differences with the jet samples, the use of the sample for $\not\!\!E_T < 50/60$ GeV is clearly discouraged. In that region a more sophisticated multivariable parameterization is needed to reduce the systematic uncertainty due to the possible influence of the topology in the selection.

Plot in Fig. 13 shows the comparison of the fitted functions (after multiplying the functions at the three levels) for the different samples and the ratio of the functions to the central one. In the ratio we compare the measured differences with the estimated uncertainty and confirm that the uncertainty covers the difference among the samples.

It should be noted that the parameterization from the *MET Back-up* sample has a small bias due to the fact that no function at Level-1 was fitted. However, since the main effect in the region of interest is coming from the Level 2 and Level 3 turn-on functions, the effect is not visible.

In the analysis we will use the parameterization obtained from the HIGH_PT_MUON sample and the quoted uncertainty to weight the MC events in the several regions under study.

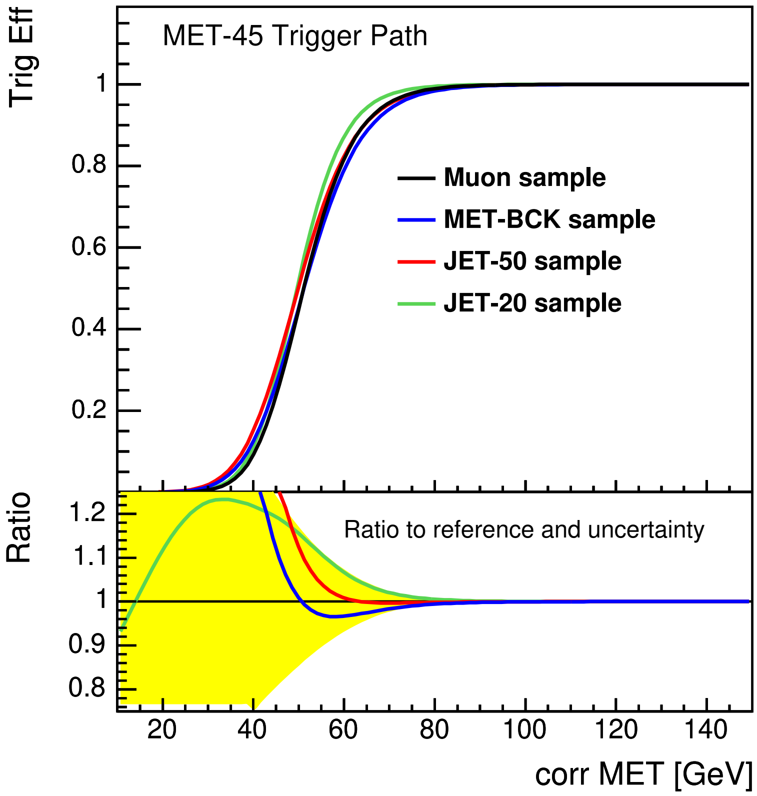

Figure 13: Total efficiency for the MET45 Trigger Path as obtained from the several samples we are using in this study. The plot below shows the ratio to the efficiency obtained with the HIGH_PT_MUON sample, which we consider our central reference. The yellow area displays the size of the uncertainty we quote on the trigger efficiency.

6 Analysis Strategy

To have the background contribution under control, i.e. understood, before "opening the box" we have followed a methodical procedure in three diferent control regions: a QCD control region, a Lepton control region and a Pre-optimization control region. Furthermore, all events in the analysis have to fulfill some Pre-selection cuts. The QCD control region was defined to estimate the multi-jet background following the MUTARE Method [10] and applying the prediction to the other control regions and finally to the signal region. The Lepton region permitted us to define a non-QCD environment with leptons in order to test our predictions in a completely different region to the signal one. Finally, the Pre-optimization region gave us the chance to test the background predictions in a signal-like environment. After that, a optimization process was made as indicated in chapter 8.

6.1 Pre-selection Cuts

Events are preselected using the following cuts:

- At least one vertex with Q $\geq$ 12 and z-component, Z_{vtx}, in the region $|Z_{vtx}| \leq$ 60 cm
- At least two jets with corrected transverse energy, $E_{T,j} \geq$ 25 GeV. Jet are reconstructed using the CDF RunI JETCLU algorithm with a radius $R = 0.4$
- At least one jet with $E_{T,j} \geq$ 35 GeV
- At least one jet is required to be central with pseudorapidity in the region, $|\eta_{jet}| \leq$ 0.9
- Corrected MET above 70 GeV
- Standard Clean up cuts for MET analysis [8]

6.2 QCD Control Region

The QCD control region is defined to be rich in multi-jet processes. Two different subregions were defined depending on the tagging requirements, only one tag or at least two tags. The following cuts are used to define this region:

- Tagging (SecVtx Tight) is required
- $\Delta\phi(MET, 2j) \leq 0.4$

This region was used to estimate the QCD from data by extracting the matrices needed for the MUTARE Method [10]. Since we were using two tagging requirements, two different matrices were needed to estimate the QCD contribution for each tagging region. To estimate the one tag contribution, a matrix built over the taggable sample was used while a different matrix built over the 1-tag + 1-taggable sample was used to estimate the double tag contribution.

6.3 Lepton Control Region

The Lepton control region is defined to test the QCD prediction [10] from data and also to test the EWK and top backgrounds. Two different subregions were defined depending on the tagging requirements, only one tag or at least two tags. The following cuts are used to define this region:

- Tagging (SecVtx Tight) is required
- $\Delta\phi(MET, 2j) \geq 0.7$
- At least one loose lepton

We define leptons as CEM electrons and loose muons with the standard definitios from the Joint Physics group listed in Table 2 and Table 3.

6.4 Pre-optimization Control Region

This region was used as a starting point for the two optimizations made in the present analysis. Two different subregions were defined depending on the tagging requirements, only one tag or at least two tags. The following cuts are used to define this region:

- Tagging (SecVtx Tight) is required
- $\Delta\phi(MET, 2j, 1j) \geq 0.7$
- $E_{T,j} \geq$ 50 GeV
- No leptons

Were leptons means CEM electrons and loose muons as described in Table 2 and Table 3.

CEM Electron selection	Cut
Transverse energy	$E_T \geqslant 10$ GeV
COT axial segments	Three or more (with 5 hits each)
COT stereo segments	Two or more (with 5 hits each)
E over P	$E/p \leqslant 2$ (or track $p_T \geqslant 50$ GeV/c)
CES fiducial	Yes
HAD over EM energy ratio	$E_{HAD}/E_{EM} \leqslant 0.055 + 0.00045 * E_{TOT}$
Track LShr	$Lshr \leqslant 0.2$ (if valid value)
CES Dz	$\lvert Dz\rvert \leqslant 3$ cm
CES Dx	$-3 \leqslant Q \times Dx \leqslant 1.5$ (cm)
CES χ^2 (strip)	$\chi^2 \leqslant 10$
Isolation	Iso(0.4)$\leqslant 0.1 \times p_T$ (for $p_T \geqslant 20$ GeV/c)
	Iso(0.4)$\leqslant 2$ GeV (for $p_T < 20$ GeV/c)

Table 2: Table of central electrons cuts.

Loose Muon selection	Cut
Transverse momentum	$p_T \geqslant 10$ GeV/c
COT axial segments	Two or more (with 5 hits each)
COT stereo segments	One or more (with 5 hits each)
COT χ^2	χ^2/ndof$\leqslant 3$
Corrected d_0	$\lvert d_{0,corr}\rvert \leqslant 0.02$ cm (with Si hits)
	$\lvert d_{0,corr}\rvert \leqslant 0.2$ cm (without Si hits)
EM energy	$E_{EM} \leqslant 2$ GeV
HAD energy	$E_{HAD} \leqslant 6$ GeV
Total CAL Energy	$E_{EM} + E_{HAD} \geqslant 0.1$ GeV
Isolation	Iso(0.4)$\leqslant 0.1 \times p_T$ (for $p_T \geqslant 20$ GeV/c)
	Iso(0.4)$\leqslant 2$ GeV (for $p_T < 20$ GeV/c)

Table 3: Table of stubless muons cuts.

7 Control Regions Results

For each Control Region described in Section 6 were obtained the number of expected and observed events detailed in Table 4 for the 1 exclusive tag selection and in Table **??** for the 1 inclusive tag selection.

The different distributions for each region are shown in the following Figures. In Figure 14, Figure 15 and Figure 16 plots of the QCD Control Region for the 1 exclusive tag selection are shown. In Figure 17, Figure 18 and Figure 19 plots of the Lepton Control Region for the 1 exclusive tag selection are shown. In Figure 20, Figure 21 and Figure 22 plots of the Lepton Control Region for the 1 exclusive tag selectionare shown.

The same set of figures are shown for the 2 inclusive tags selection. In Figure 23, Figure 24 and Figure 25 plots of the QCD Control Region for the 2 inclusive tags selection are shown. In Figure 26, Figure 27 and Figure 28 plots of the Lepton Control Region for the 2 inclusive tags selection are shown. In Figure 29, Figure 30 and Figure 31 plots of the Lepton Control Region for the 2 inclusive tags selectionare shown.

CDF Run II Preliminary

1 Exclusive Tag	QCD Region	Lepton Region	Preoptimization Region
Boson production	84 ± 36	132 ± 57	376 ± 162
Diboson production	4 ± 1	20 ± 5	41 ± 10
Top pair production	60 ± 15	371 ± 93	478 ± 119
Single top production	5 ± 1	34 ± 8	45 ± 11
HF QCD Multijets	9741 ± 4870	195 ± 97	1660 ± 830
Light-flavour contamination	5430 ± 2226	190 ± 78	919 ± 377
Total expected	15325 ± 3525	943 ± 217	3520 ± 810
Observed (2.5 fb^{-1})	15390	890	3525

Table 4: Table of predicted and observed events in the control regions (1 exclusive tag selection).

CDF Run II Preliminary

2 Inclusive Tags	QCD Region	Lepton Region	Preoptimization Region
Boson production	10 ± 7	19 ± 14	29 ± 22
Diboson production	0.4 ± 0.1	2 ± 0.6	4 ± 1
Top pair production	18 ± 6	107 ± 34	140 ± 45
Single top production	1 ± 0.2	4 ± 1	6 ± 1
HF QCD Multijets	864 ± 432	23 ± 11	273 ± 136
Light-flavour contamination	238 ± 48	8 ± 2	57 ± 11
Total expected	1132 ± 226	164 ± 33	510 ± 102
Observed (2.5 fb^{-1})	1104	156	455

Table 5: Table of predicted and observed events in the control regions (2 inclusive tag selection).

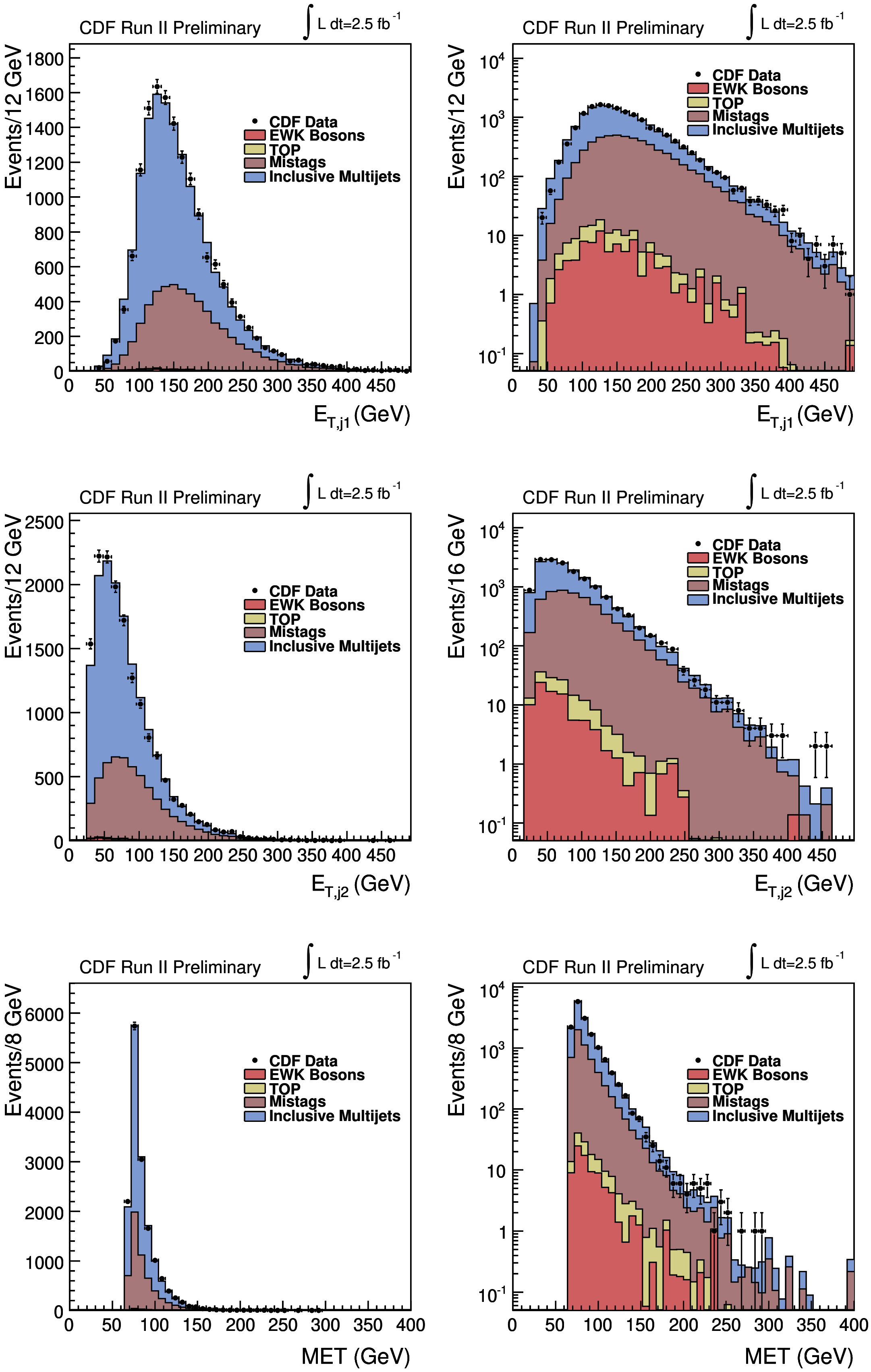

Figure 14: First jet E_T, second jet E_T and $\not{E}_T$ in the QCD Control Region (1 exclusive tag), linear and logarithmic scale.

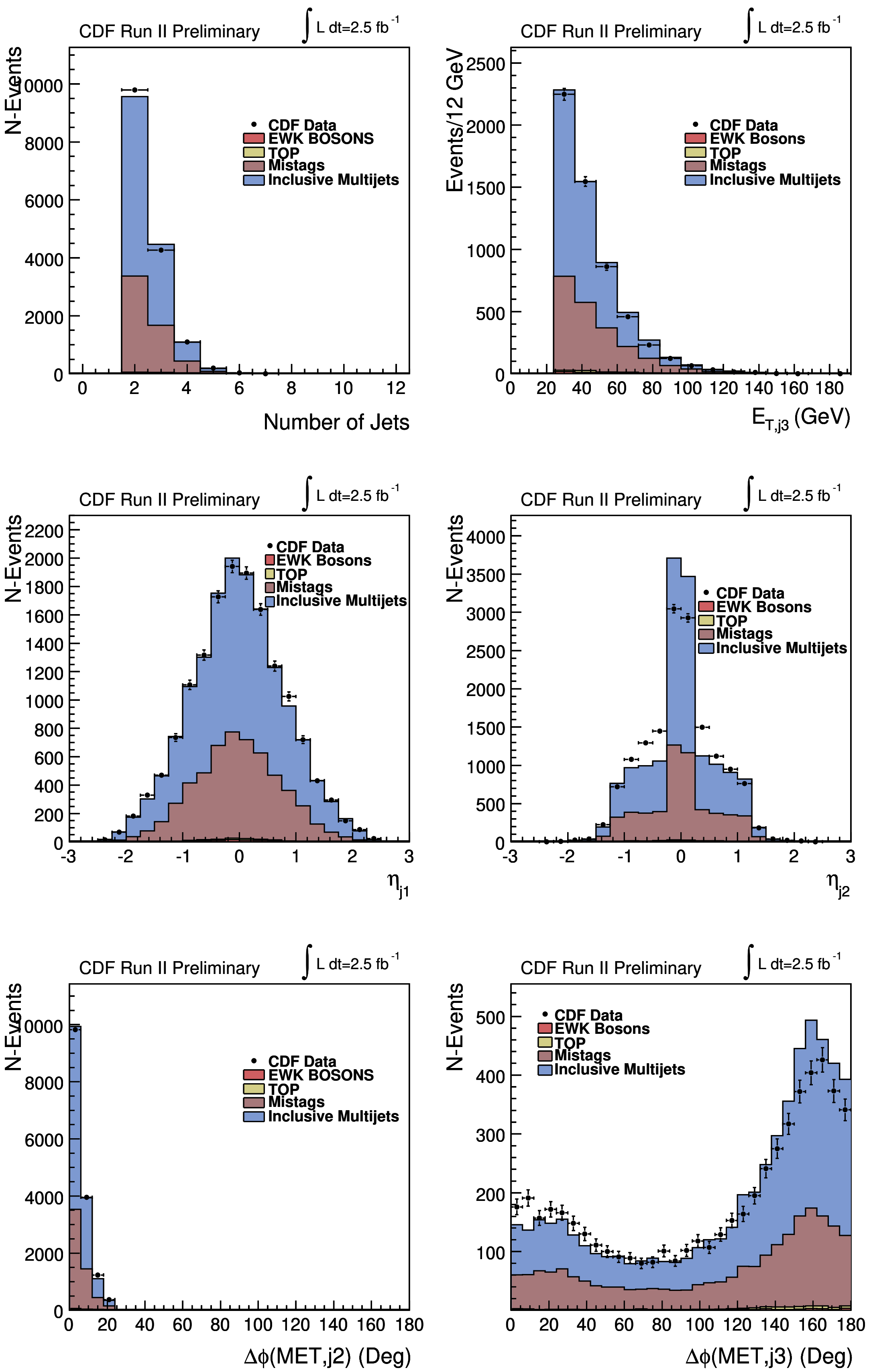

Figure 15: Number of jets, third jet E_T, first jet η, second jet η, $\Delta\phi(MET, 2j)$ and $\Delta\phi(MET, 3j)$ in the QCD Control Region (1 exclusive tag).

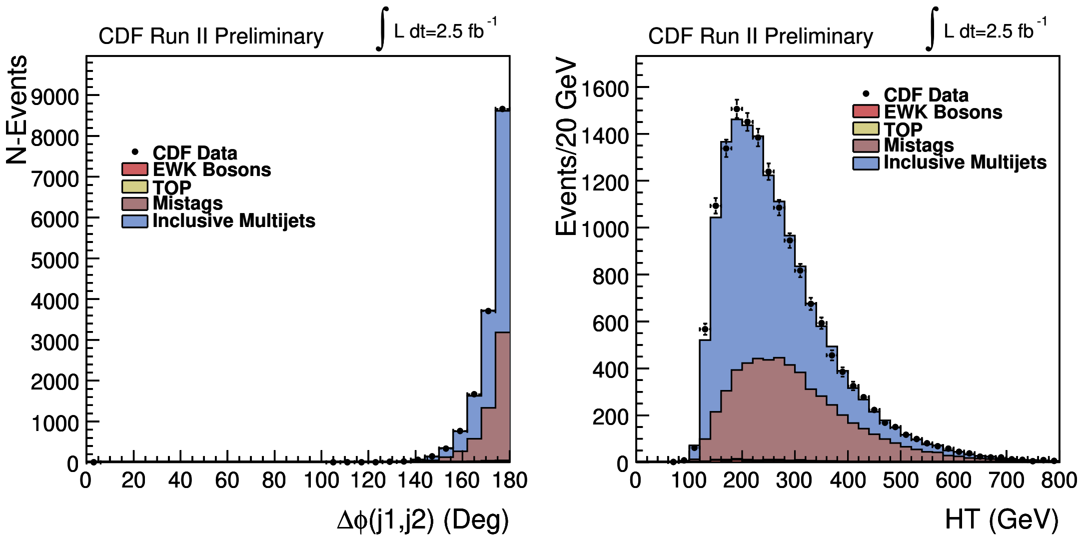

Figure 16: $\Delta\phi(1j, 2j)$ and HT in the QCD Control Region (1 exclusive tag).

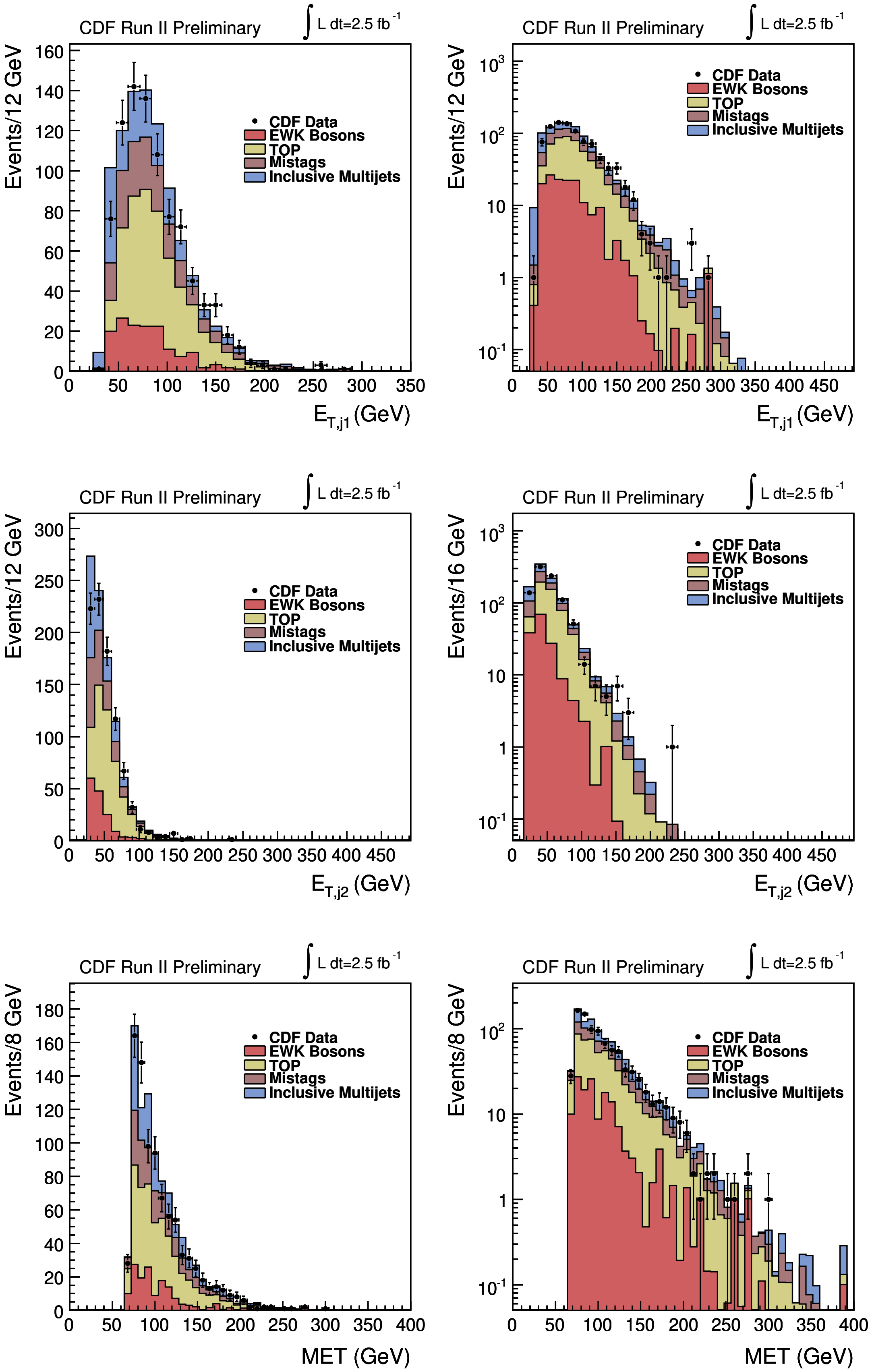

Figure 17: First jet E_T, second jet E_T and $\not\!\!E_T$ in the Lepton Control Region (1 exclusive tag), linear and logarithmic scale.

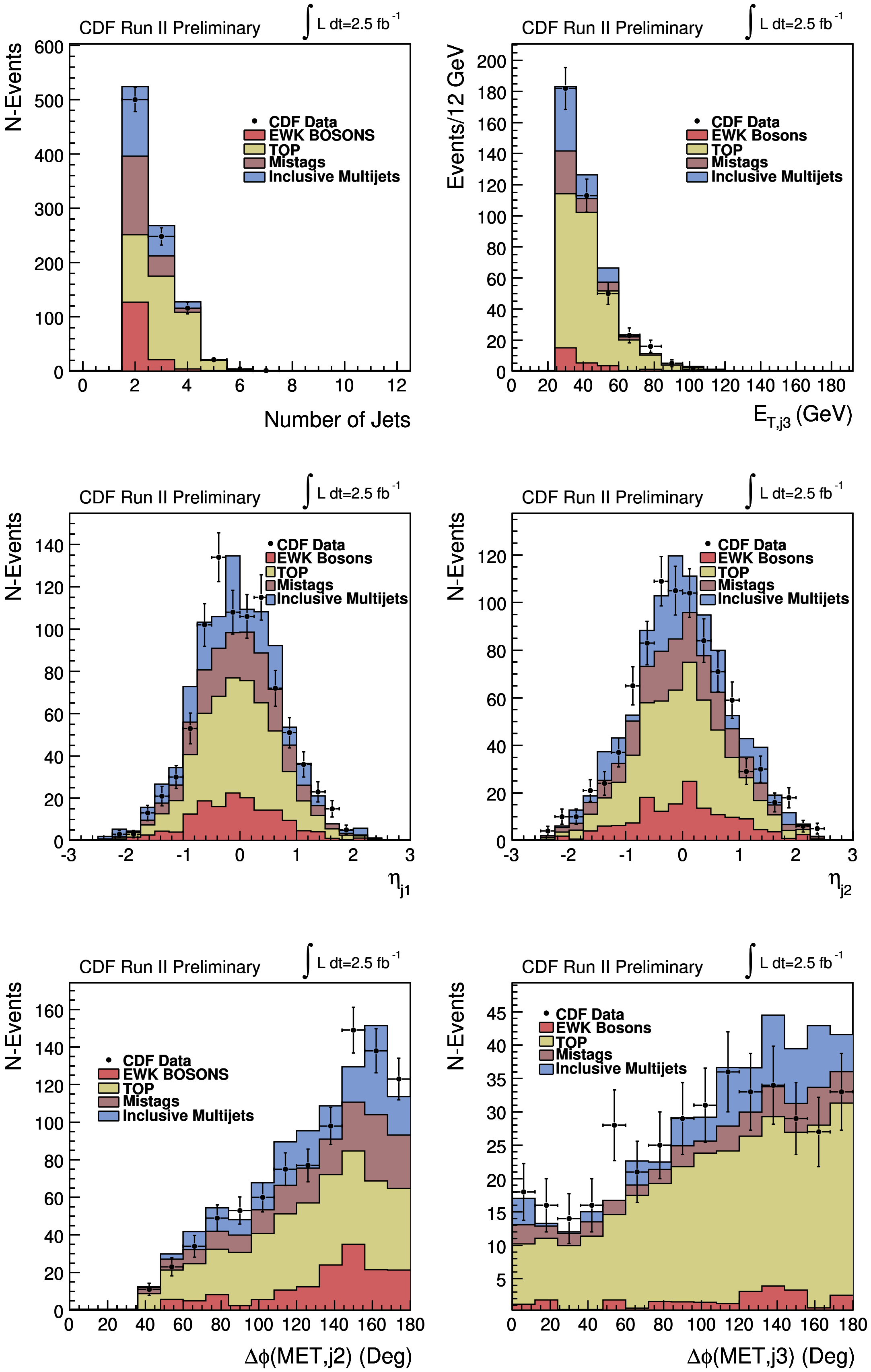

Figure 18: Number of jets, third jet E_T, first jet η, second jet η, $\Delta\phi(MET, 2j)$ and $\Delta\phi(MET, 3j)$ in the Lepton Control Region (1 exclusive tag).

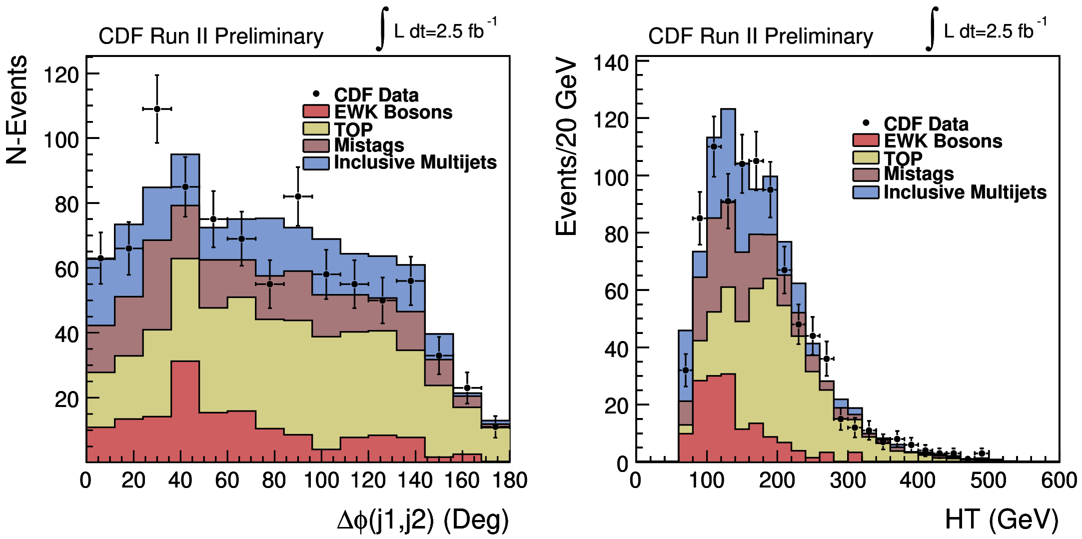

Figure 19: $\Delta\phi(1j, 2j)$ and HT in the Lepton Control Region (1 exclusive tag).

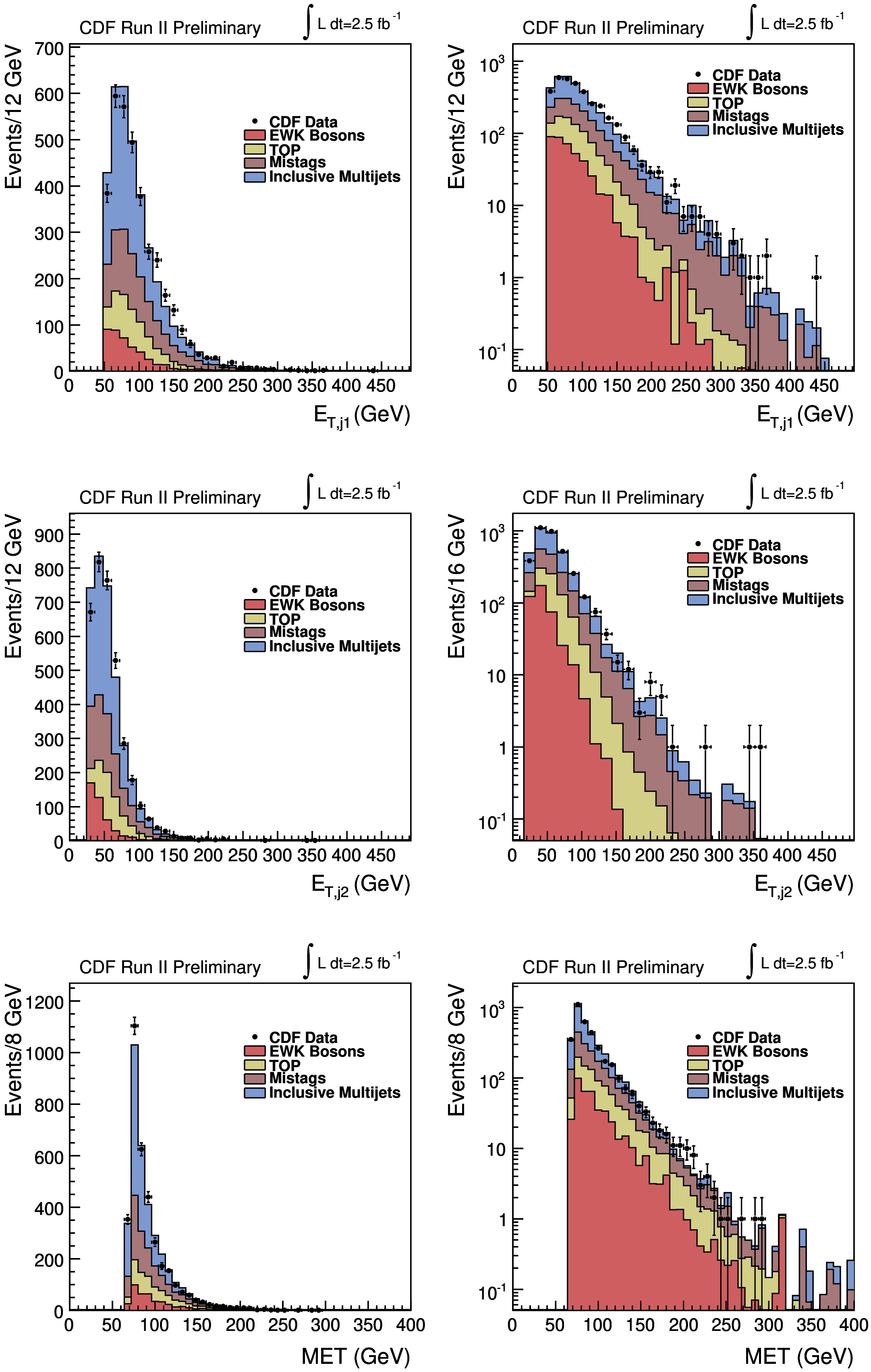

Figure 20: First jet E_T, second jet E_T and $\not{E}_T$ in the Pre-Optimization Region (1 exclusive tag), linear and logarithmic scale.

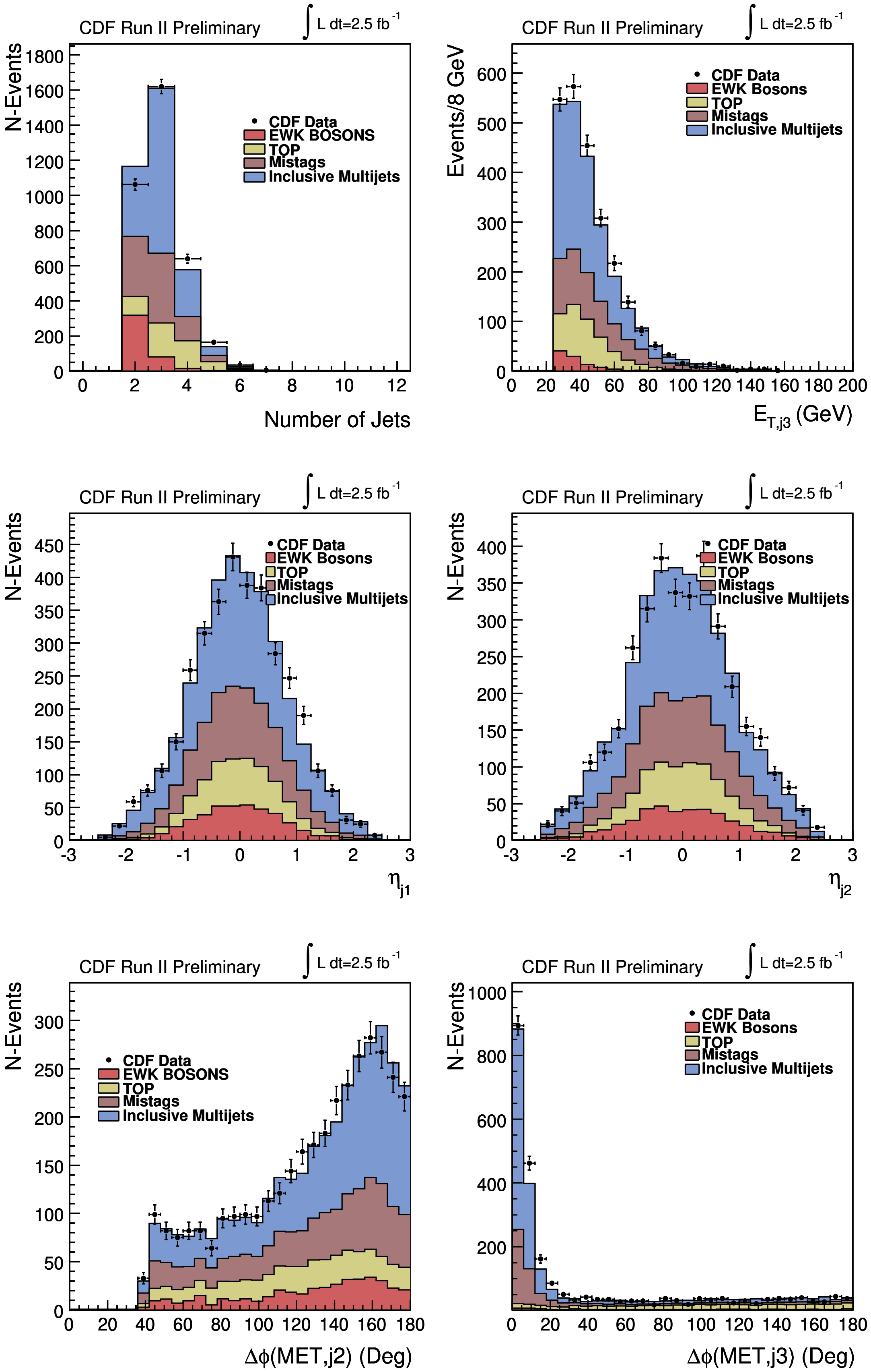

Figure 21: Number of jets, third jet E_T, first jet η, second jet η, $\Delta\phi(MET, 2j)$ and $\Delta\phi(MET, 3j)$ in the Pre-Optimization Control Region (1 exclusive tag).

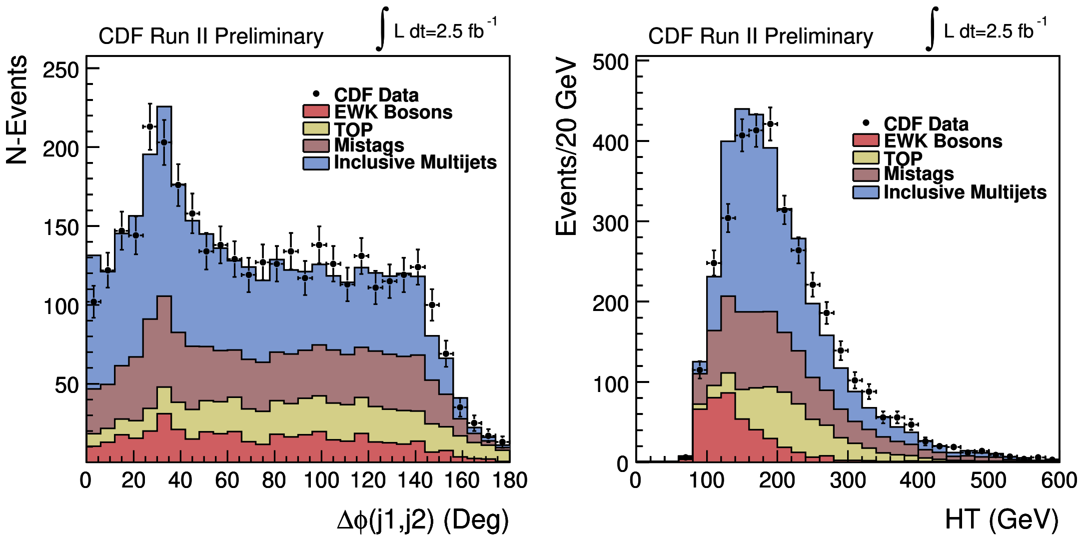

Figure 22: $\Delta\phi(1j, 2j)$ and HT in the Pre-Optimization Control Region (1 exclusive tag).

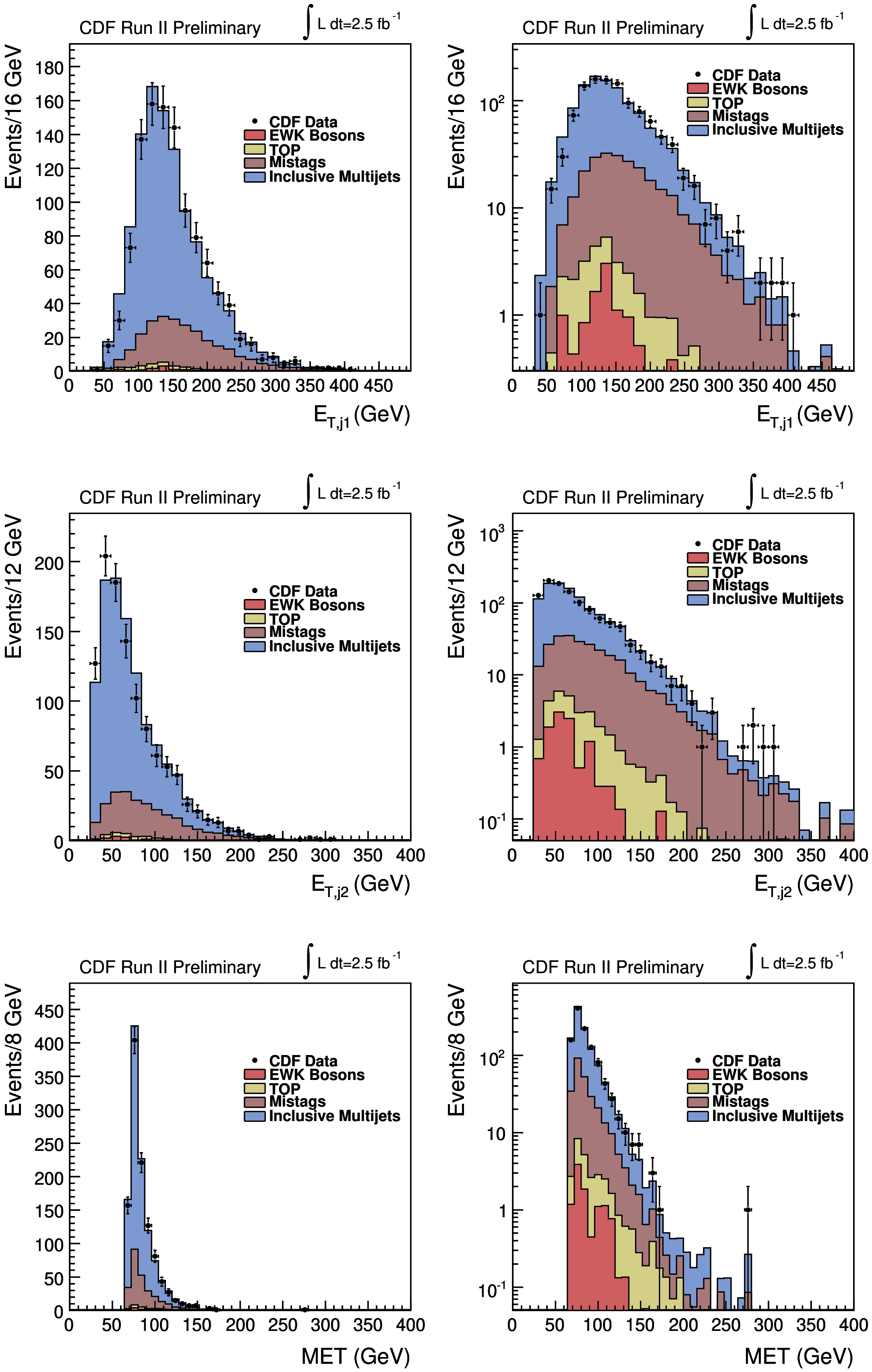

Figure 23: First jet E_T, second jet E_T and $\not{E}_T$ in the QCD Control Region (2 inclusive tags), linear and logarithmic scale.

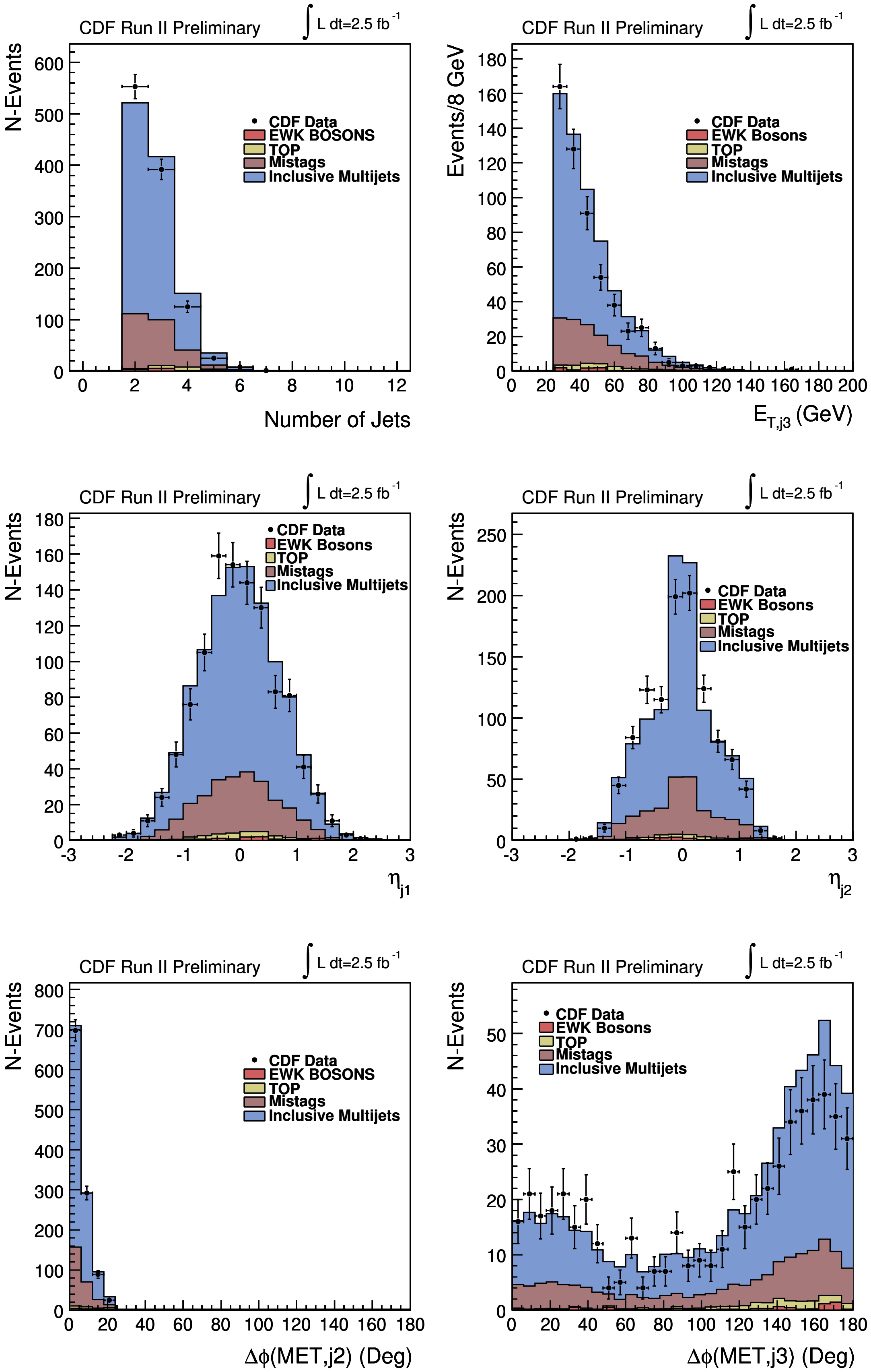

Figure 24: Number of jets, third jet E_T, first jet η, second jet η, $\Delta\phi(MET, 2j)$ and $\Delta\phi(MET, 3j)$ in the QCD Control Region (2 inclusive tags).

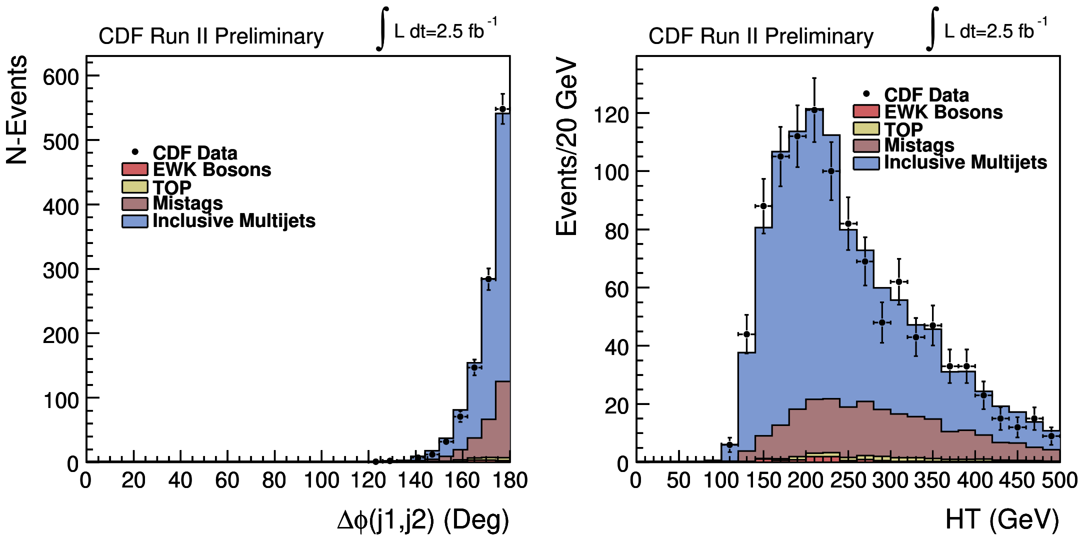

Figure 25: $\Delta\phi(1j, 2j)$ and HT in the QCD Control Region (2 inclusive tags).

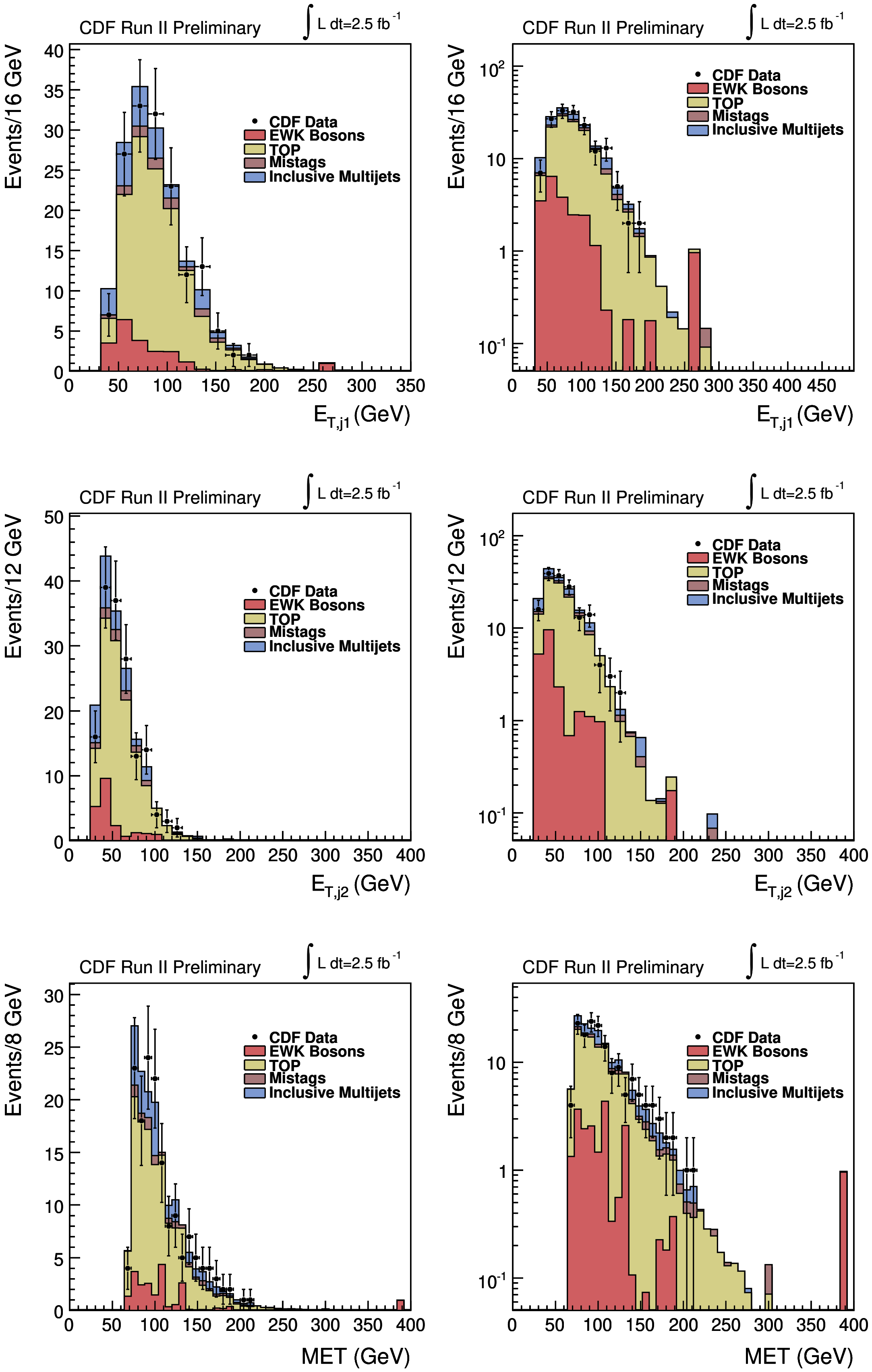

Figure 26: First jet E_T, second jet E_T and $\not\!\!E_T$ in the Lepton Control Region (2 inclusive tags) linear and logarithmic scale.

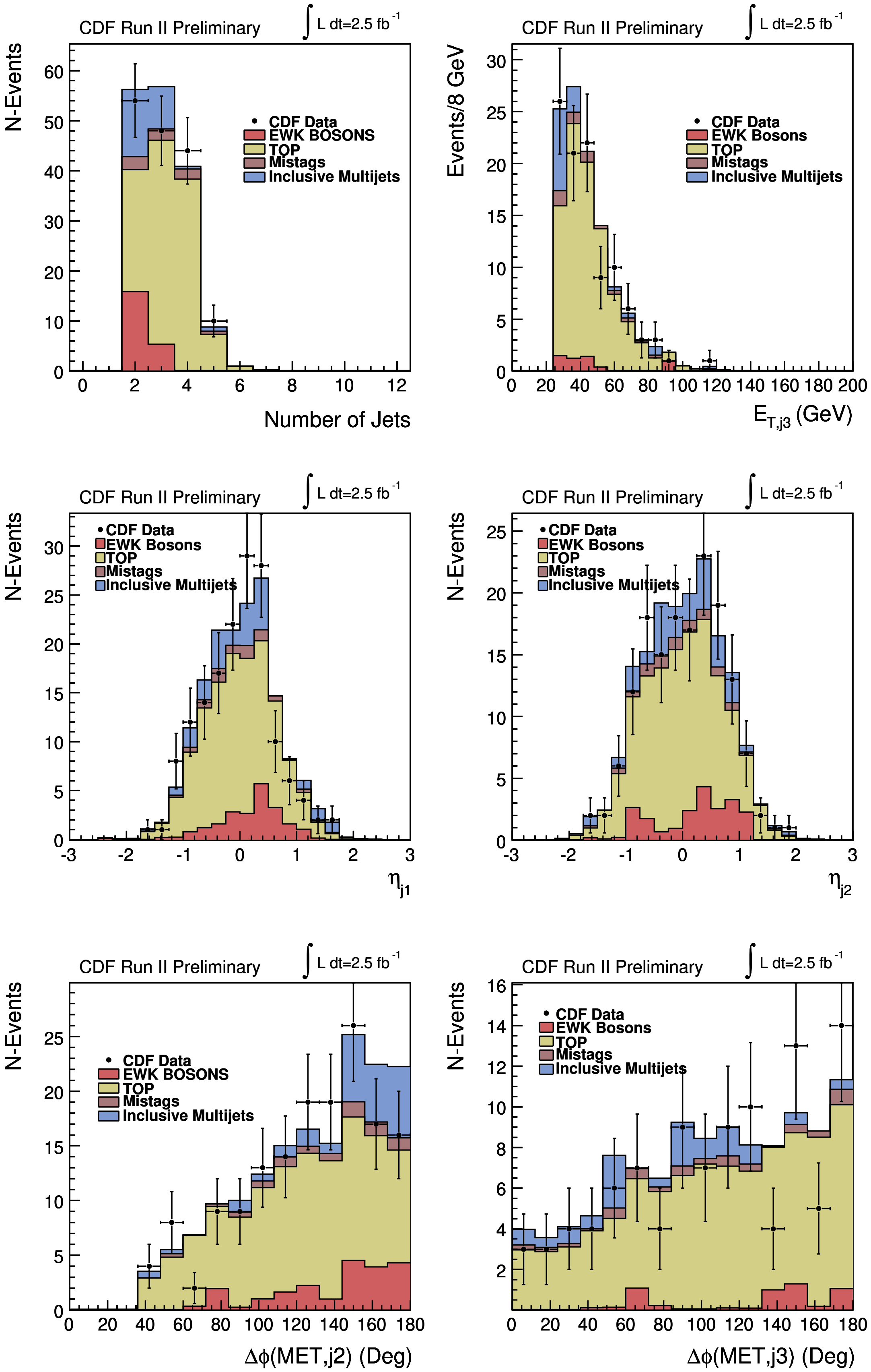

Figure 27: Number of jets, third jet E_T, first jet η, second jet η, $\Delta\phi(MET, 2j)$ and $\Delta\phi(MET, 3j)$ in the Lepton Control Region (2 inclusive tags).

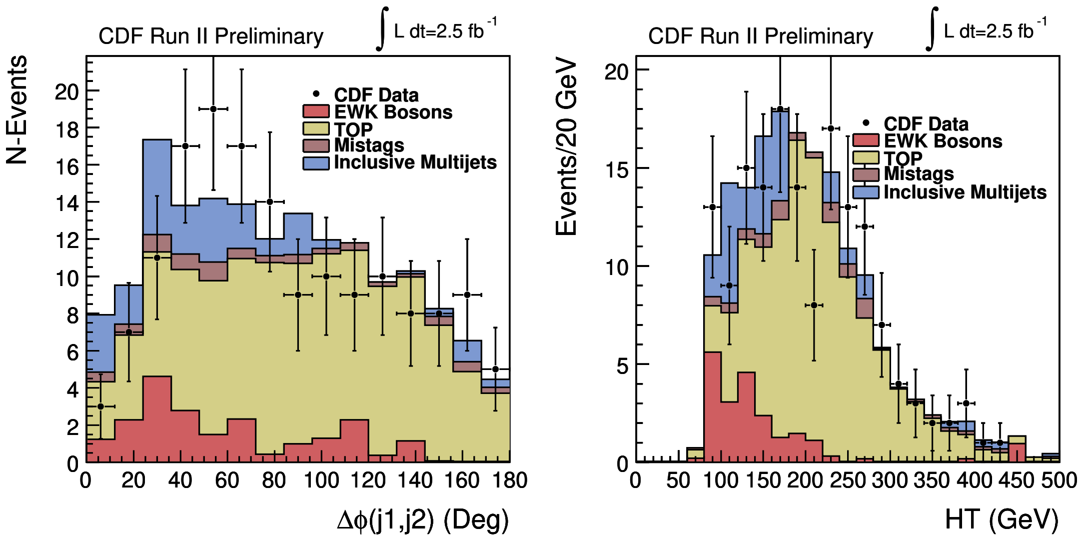

Figure 28: $\Delta\phi(1j, 2j)$ and HT in the Lepton Control Region (2 inclusive tags).

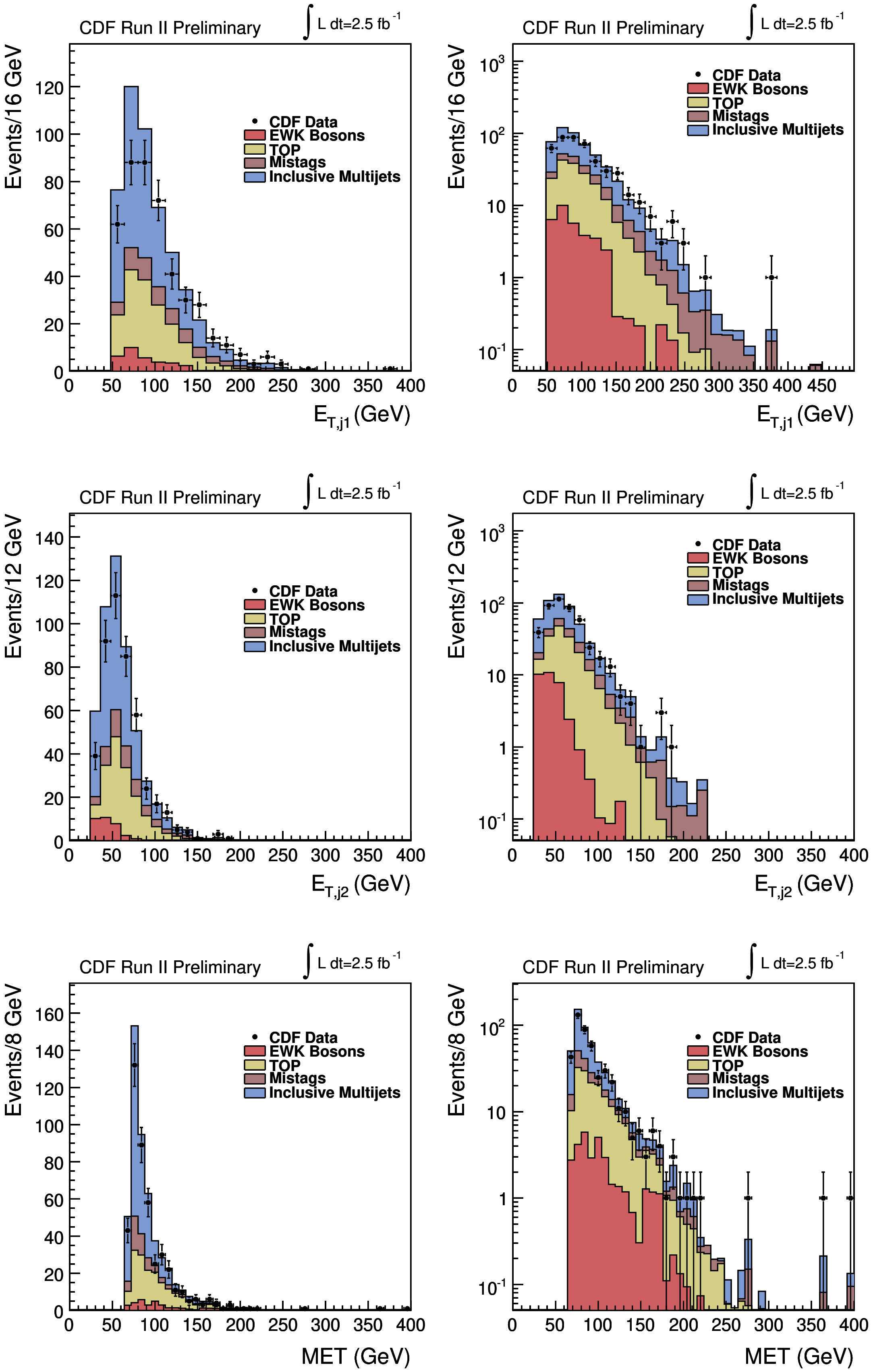

Figure 29: First jet E_T, second jet E_T and $\not{E}_T$ in the Pre-Optimization Region (2 inclusive tags), linear and logarithmic scale.

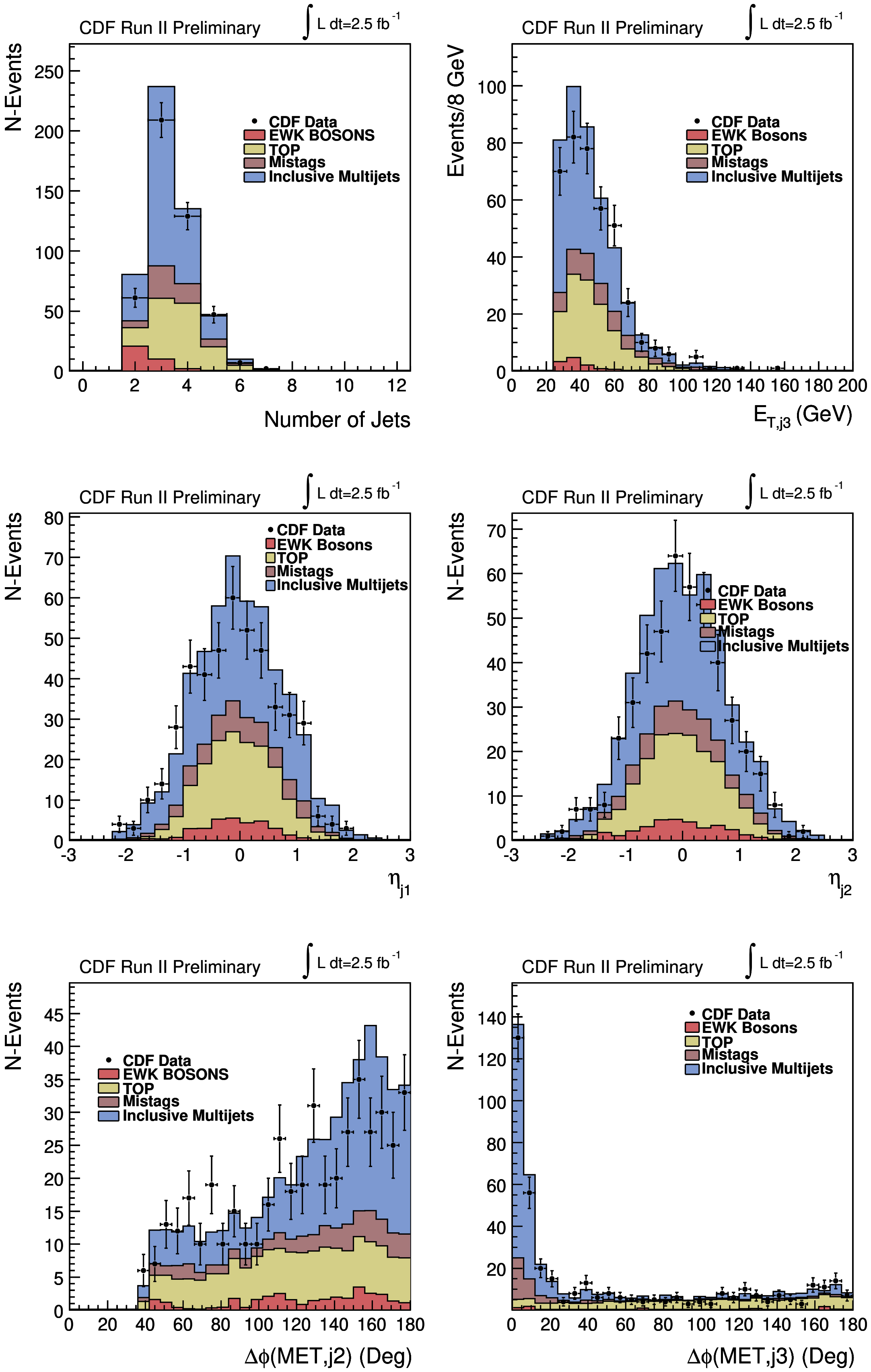

Figure 30: Number of jets, third jet E_T, first jet η, second jet η, $\Delta\phi(MET, 2j)$ and $\Delta\phi(MET, 3j)$ in the Pre-Optimization Control Region (2 inclusive tags).

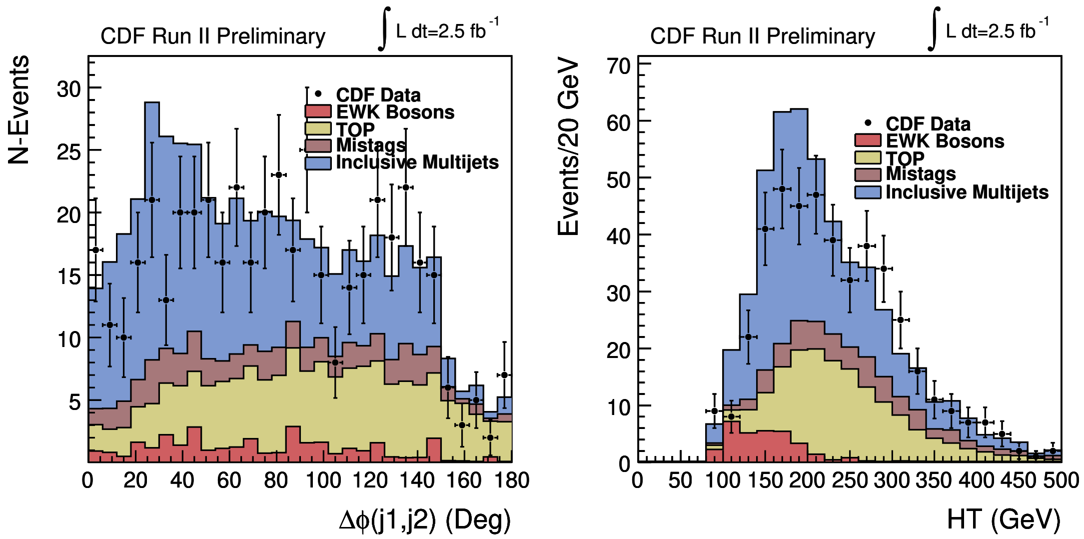

Figure 31: $\Delta\phi(1j, 2j)$ and HT in the Pre-Optimization Control Region (2 inclusive tags).

8 Signal Optimization

In order to reduce the background contribution we perform an optimization process via two different NN over two different SUSY points. The two points were chosen to have a large and small mass difference between the gluino and the sbottom. With this SUSY points two well differentiated kinematic behaviors were covered in each optimization.

The two selected points are:

- PA (Large Δm): M($\tilde{g}$) = 335 GeV/c^2, M($\tilde{b}$) = 260 GeV/c^2, M($\tilde{\chi}$) = 60 GeV/c^2
- PB (Small Δm): M($\tilde{g}$) = 335 GeV/c^2, M($\tilde{b}$) = 315 GeV/c^2, M($\tilde{\chi}$) = 60 GeV/c^2

The optimization process takes as a benchmark the Pre-optimization selection, described in Section 6.4. In addiction, for the Large Δm optimization a cut on the number of jets grater than two was applied. For the Small Δm optimization this cut was not applied because of the small amount of energy available in the gluino decay which implies a softer jet multiplicity in the final estate. Over this selection, a first NN was applied to distinguish between gluino signal and QCD Multijets background. This first NN was trained with signal MC versus taggable jets (QCD-like) over the Pre-optimization region with 1 exclusive tag in order to have enough statistics. A second NN was applied to remove the remaining backgrounds, mainly $t\bar{t}$ production at this point. This NN was training with signal MC versus $t\bar{t}$ MC also over the Pre-optimization region with 1 exclusive tag.

The previous process was made for the two different SUSY points as well as for 1 exclusive and 2 inclusive tag selection.

8.1 Neural Network Architecture

All the NN used in the present analysis were trained and tested using the TMVA package. The same structure was used for the 4 NN, consisting in two layers with n+1 and n nodes where n is the number of variables, and one output node. As an architecture example Figure 32 shows the particular case of the QCD Multijets vs PA signal NN.

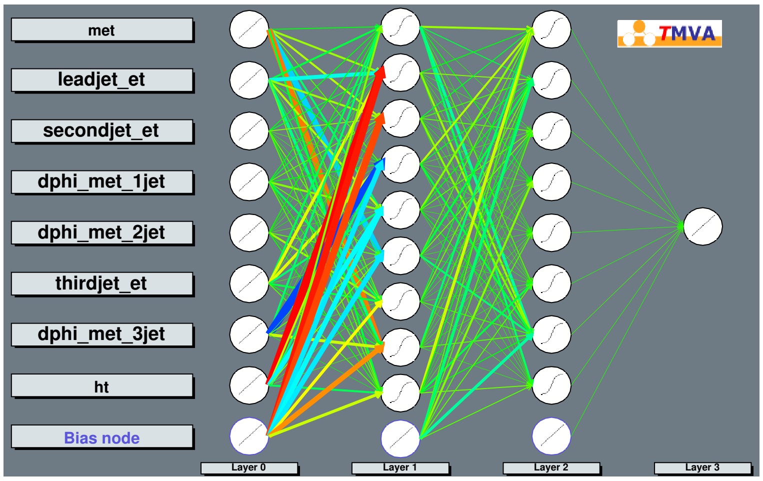

Figure 32: NN's architecture used for the training, in particular for the one used to distinguish QCD background from PA gluino signal.

In the following subsections will be shown the input variables, the training and test results for each NN. The same set of variables were used in the QCD based and top based NN with slightly differences for the PA and PB signal purposes. This variables were found as the ones with better distinction power and are almost the same that in the previous version of this analysis with 1.8 fb^{-1}. As it is shown in Section 6.4 all this variables are well modeled in the Pre-optimization region.

The input variables for the PA optimization are:

- $\not{E}_T$
- $E_{T,j1}$
- $E_{T,j2}$
- $E_{T,j3}$
- $\Delta\phi(MET, j1)$
- $\Delta\phi(MET, j2)$
- $\Delta\phi(MET, j3)$
- HT

The input variables for the PB optimization are:

- $\not{E}_T$
- $E_{T,j1}$
- $E_{T,j2}$
- $\Delta\phi(MET, j1)$
- $\Delta\phi(MET, j2)$
- $Min\ \Delta\phi(MET, jets)$
- HT

8.1.1 QCD Multijets Neural Networks

The distributions of the imput variables used in for the QCD Multijet vs PA signal and QCD Multijet vs PB signal Neural Networks are shown in Figure 33 and Figure 34 respectively.

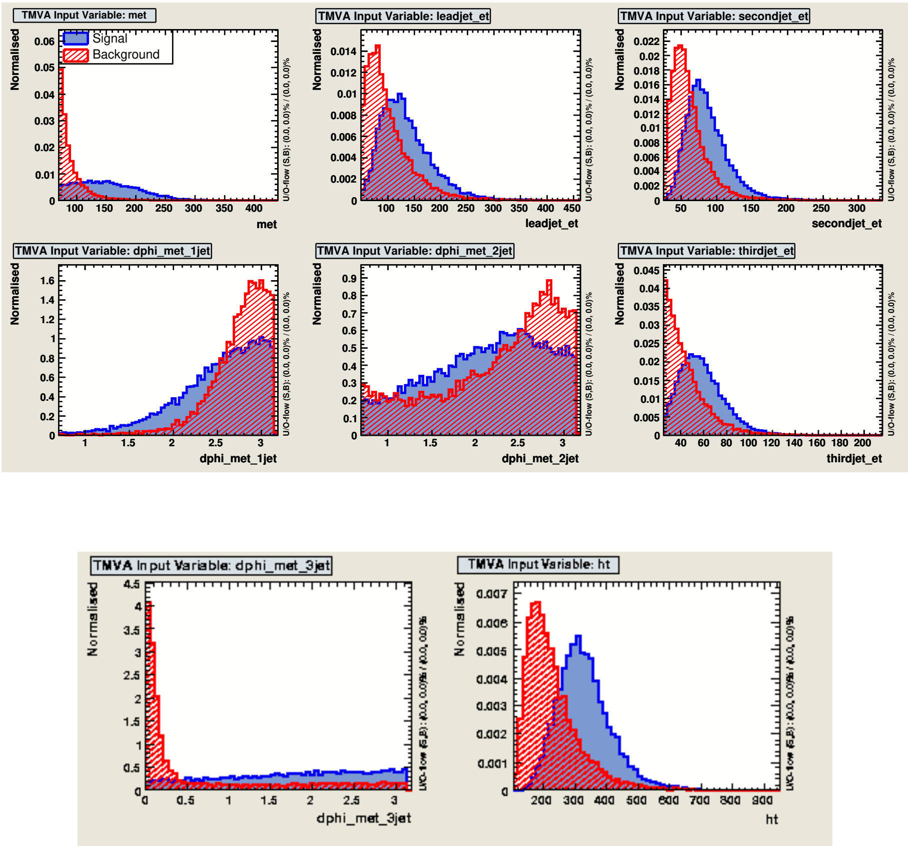

Figure 33: Input variables used for the training in the QCD Multijets vs PA signal Neural Network

After choose the set of variables used as input for the NN a training and test processes were made with the TMVA package. This process was perform over the Pre-optimization region with 1 exclusive tag. Signal MC and taggable jets (QCD-like) were provided to NN as training targets. Figure 35 shows the NN output comparison between the training and test sample for the both PA and PB signal points. The agreement between the two test and train outputs is an indicative of no over-training.

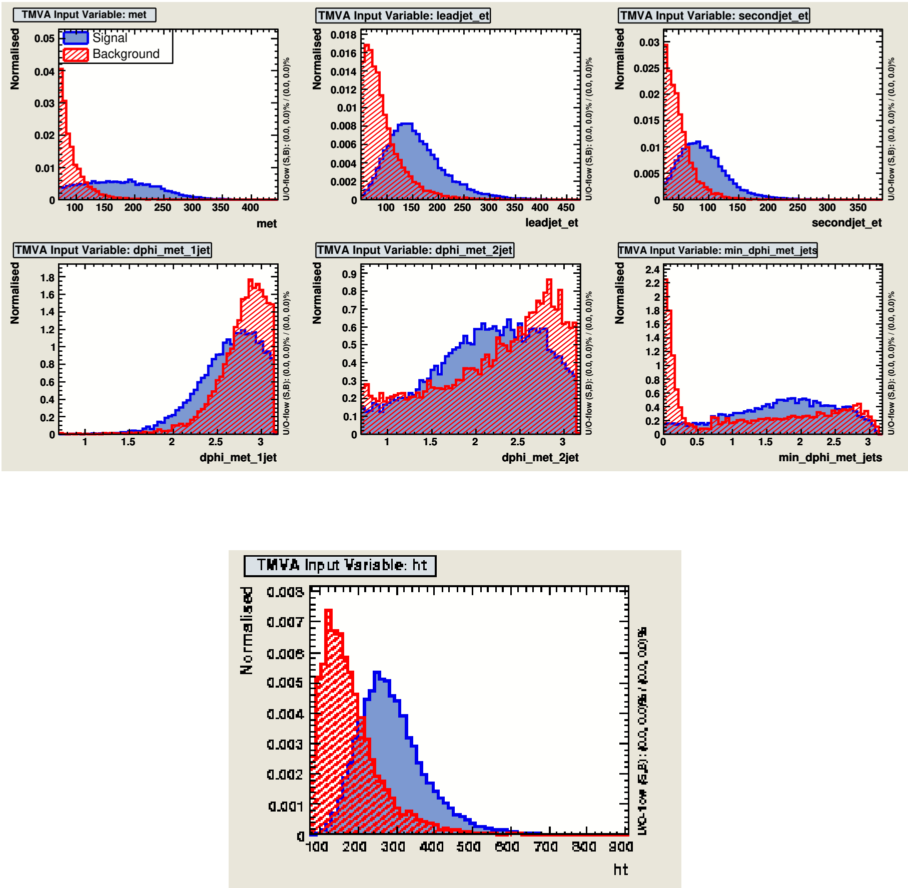

Figure 34: Input variables used for the training in the QCD Multijets vs PB signal Neural Network

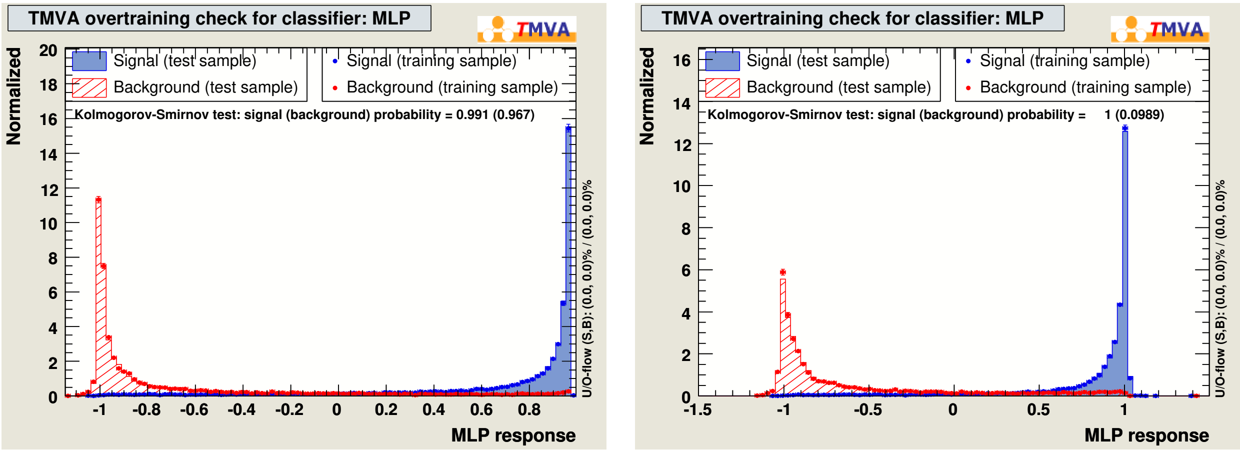

Figure 35: QCD Multijet NN training and test output for the PA (left) and PB (right) signal points

8.1.2 Top pair Neural Networks

The distributions of the imput variables used in for the Top pair vs PA signal and Top pair vs PB signal Neural Networks are shown in Figure 36 and Figure 37 respectively.

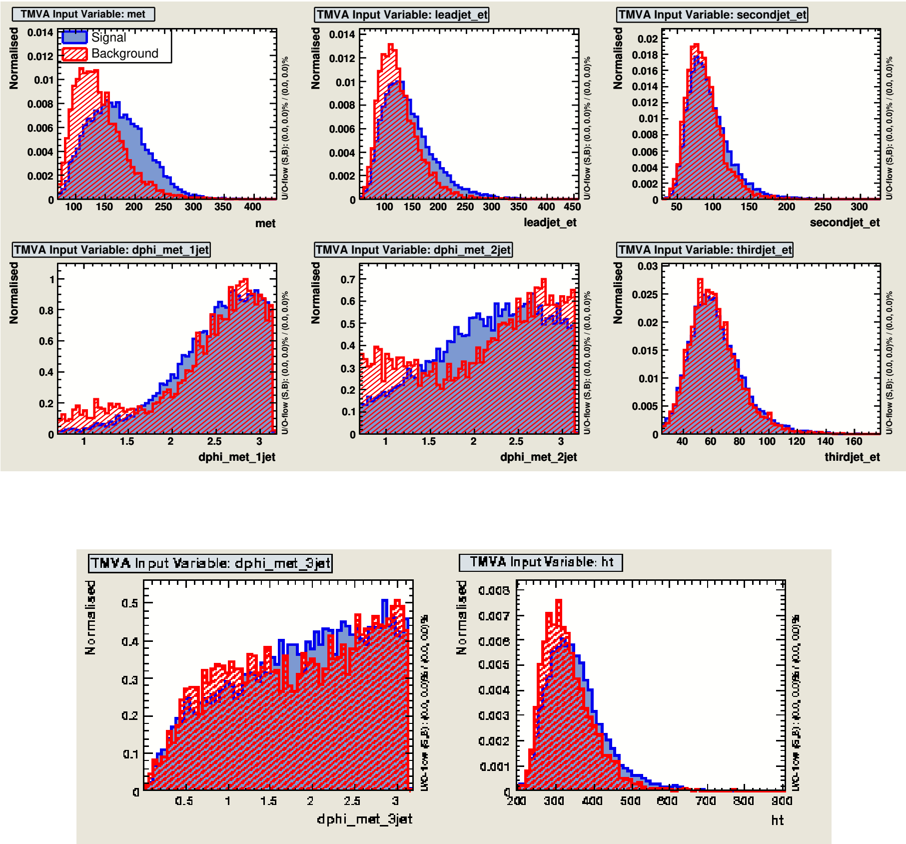

Figure 36: Input variables used for the training in the Top pair vs PA signal Neural Network

After choose the set of variables used as input for the NN a training and test processes were made with the TMVA package. As in the other NN the training process was perform over the Pre-optimization region with 1 exclusive tag. In this case signal MC and $t\bar{t}$ MC were provided to NN as training targets. Figure 35 shows the NN output comparison between the training and test sample for the both PA and PB signal points. The agreement between the two test and train outputs is an indicative of no over-training.

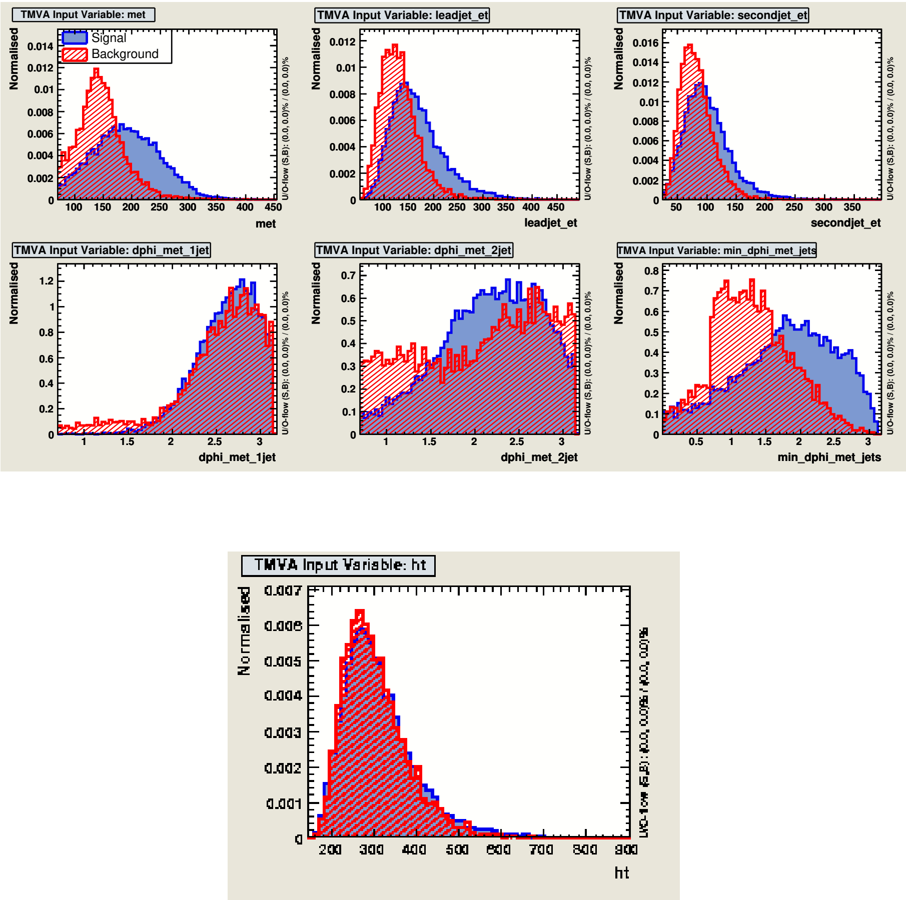

Figure 37: Input variables used for the training in the Top pair vs PB signal Neural Network

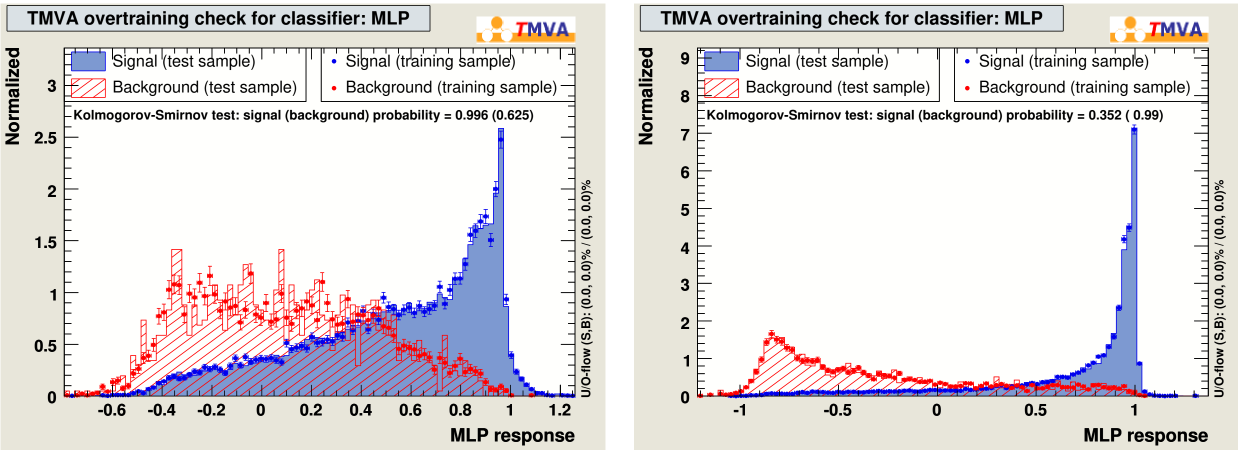

Figure 38: Top pair NN training and test output for the PA (left) and PB (right) signal points

8.2 QCD Multijets Neural Network Results

By applying to the Pre-optimization region the QCD Multijets Neural Networks described in the previous section we obtained the outputs showed in Figure 39 for the PA optimization with 1 exclusive tag and 2 inclusive tags. Figure 40 shows the QCD Multijets Neural Networks output for the PB optimization with 1 exclusive tag and 2 inclusive tags.

For all the cases showed in Figure 39 and Figure 40 we found an optimal selection cut on 0.8 in the Neural Network's output. With this cut we got a good $S/sqrtB$ keeping a reasonable amount of signal.

In Figure 41 the four QCD Multijets NN's outputs are shown with the systematic error on the background prediction.

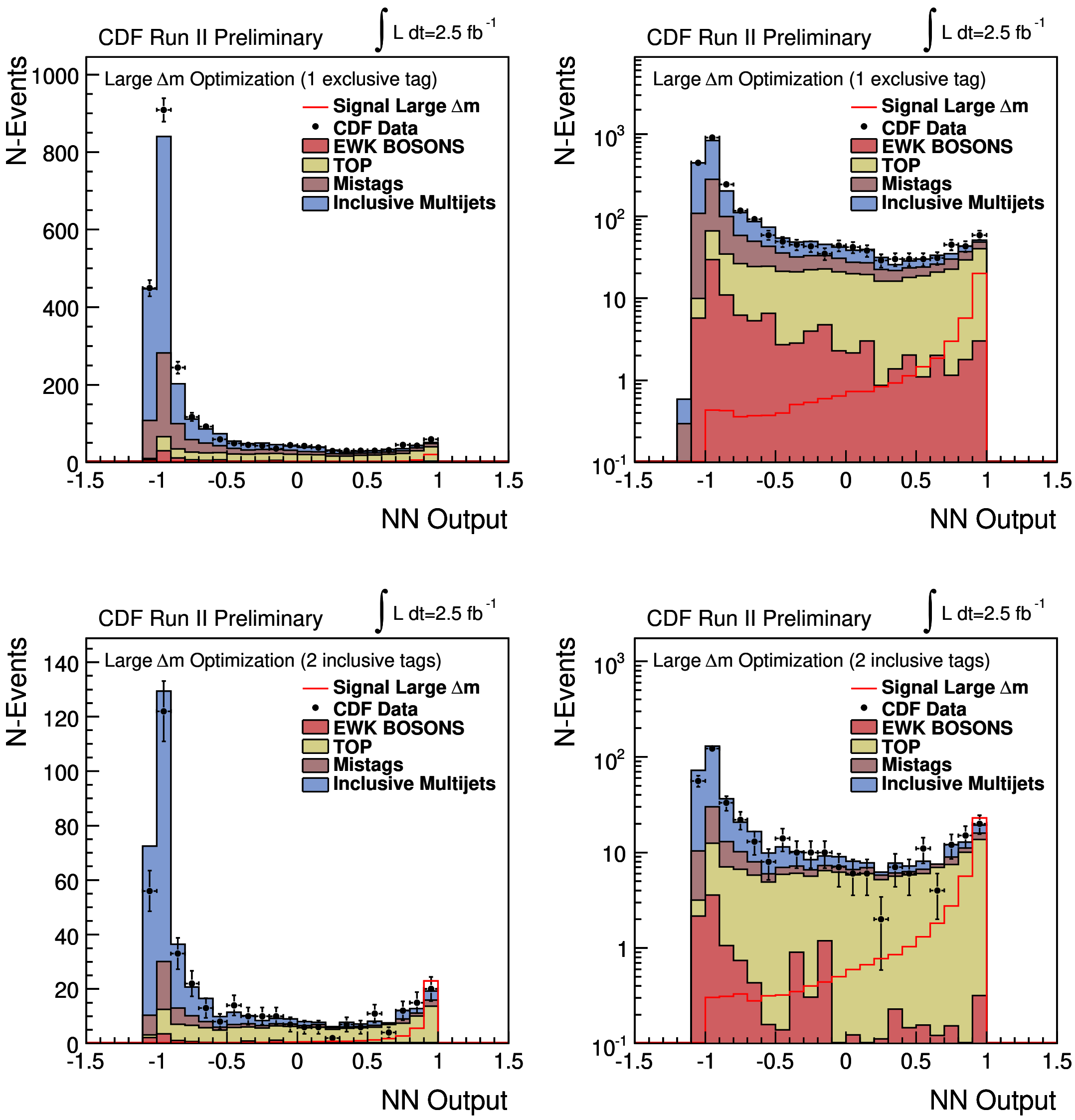

Figure 39: QCD Neural Network output plots for the Large Δm signal point with 1 exclusive tag (top) and 2 inclusive tags (bottom)

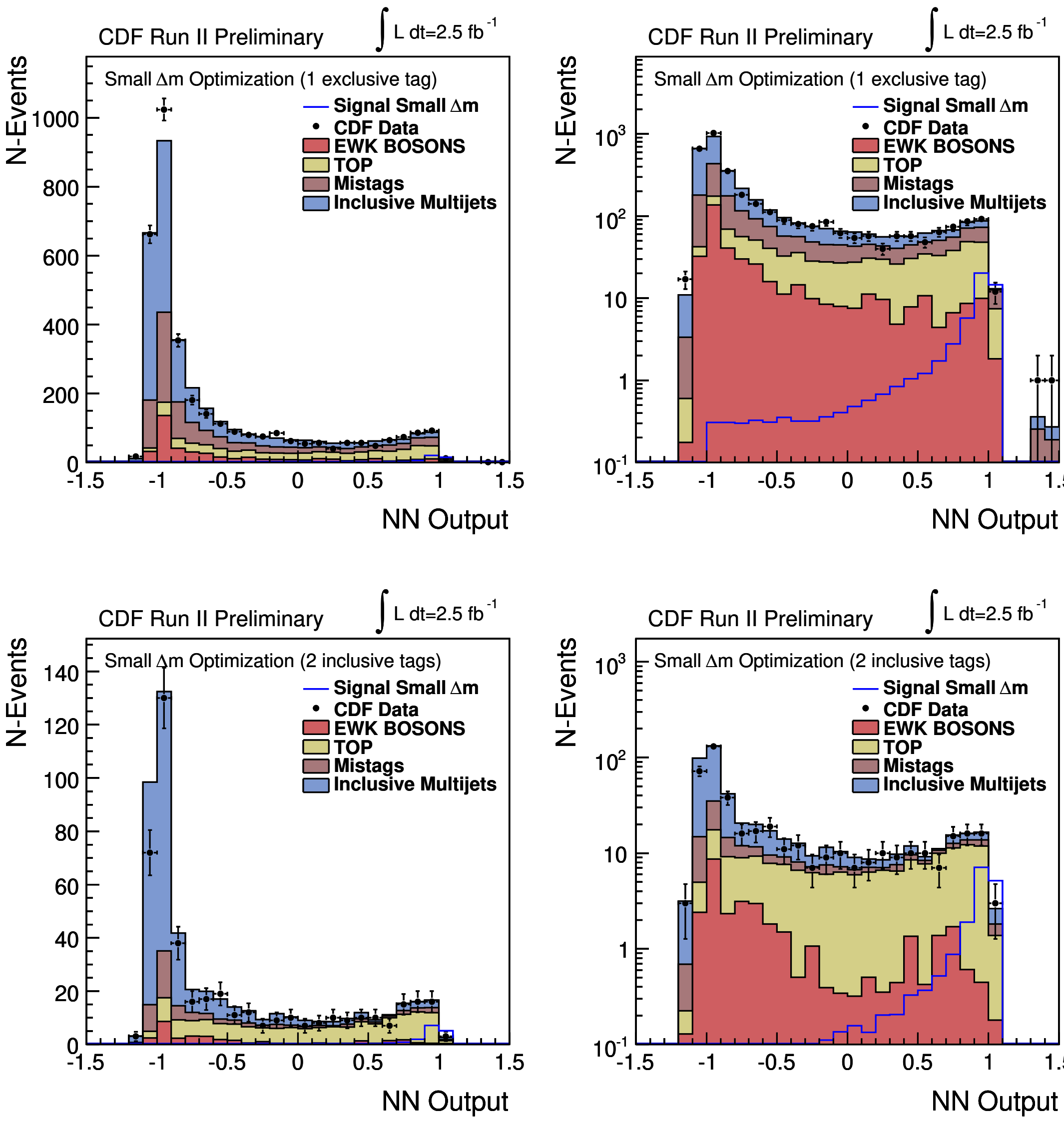

Figure 40: QCD Neural Network output plots for the Small Δm signal point with 1 exclusive tag (top) and 2 inclusive tags (bottom)

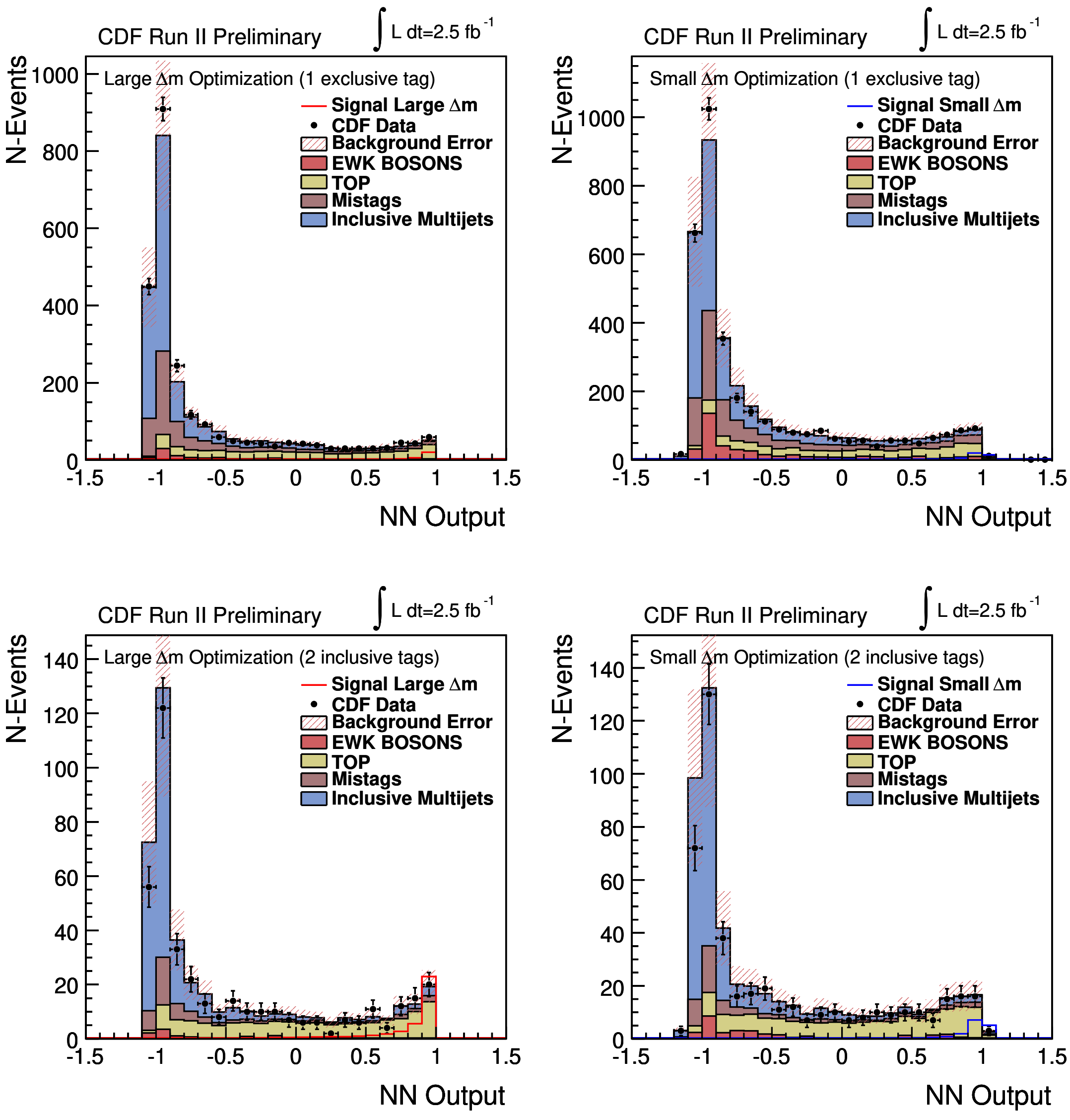

Figure 41: QCD Neural Network output plots for the Large Δm and Small Δm signal point with 1 exclusive tag (top) and 2 inclusive tags (bottom) including the background errors

8.3 Top pair Neural Network Results

At this stage of the optimization we apply the second Neural Network, based on top pair discrimination, to the events obtained after the cut on 0.8 on the output of the QCD Multijets Neural Network. The result of appliying the top pair NN to this events is shown in Figure 42 for the PA optimization and Figure 43 for the PB optimization.

We found 0.6 an optimal selection cut in the PA optimization Neural Network's output and 0.8 selection cut in the PB optimization Neural Network's output.

Figure 44 shows the $S/sqrtB$ for all the optimization and the cut applied in each one plotted as an arrow. Other signal points are shown in the figure, confirming the strength of the cut.

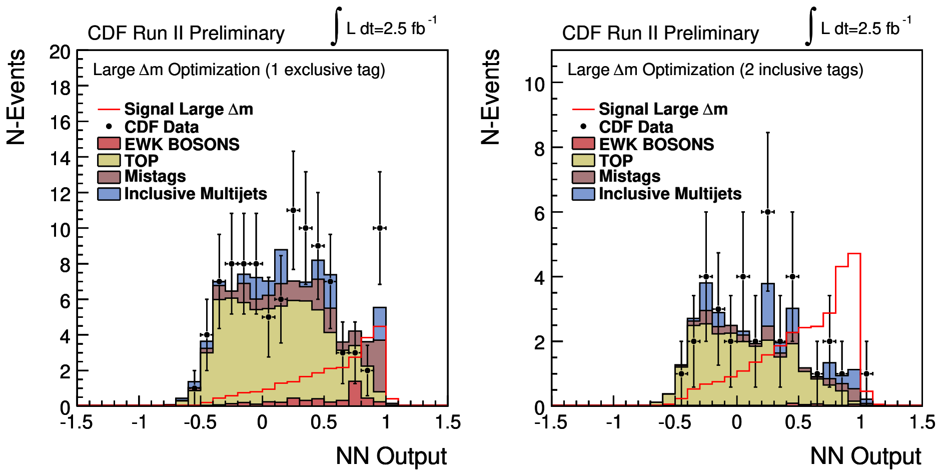

Figure 42: Top Neural Network output plots for the Large Δm signal point with 1 exclusive tag (left) and 2 inclusive tags (right)

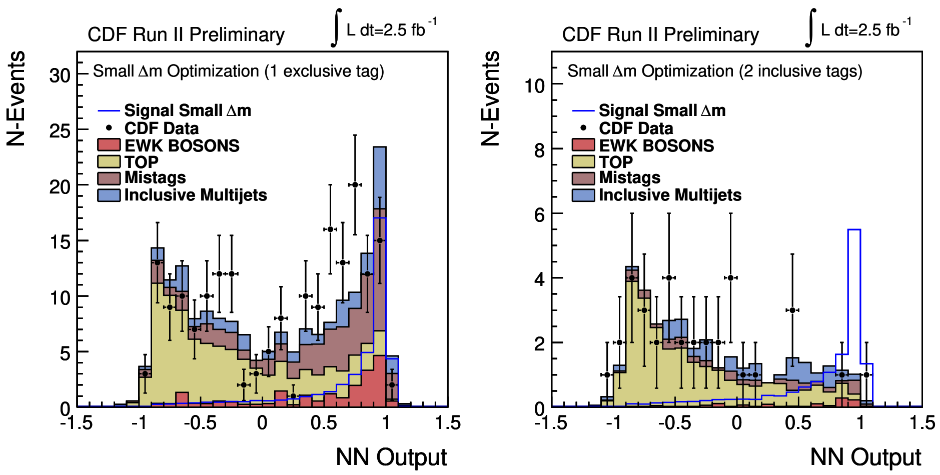

Figure 43: Top Neural Network output plots for the Small Δm signal point with 1 exclusive tag (left) and 2 inclusive tags (right)

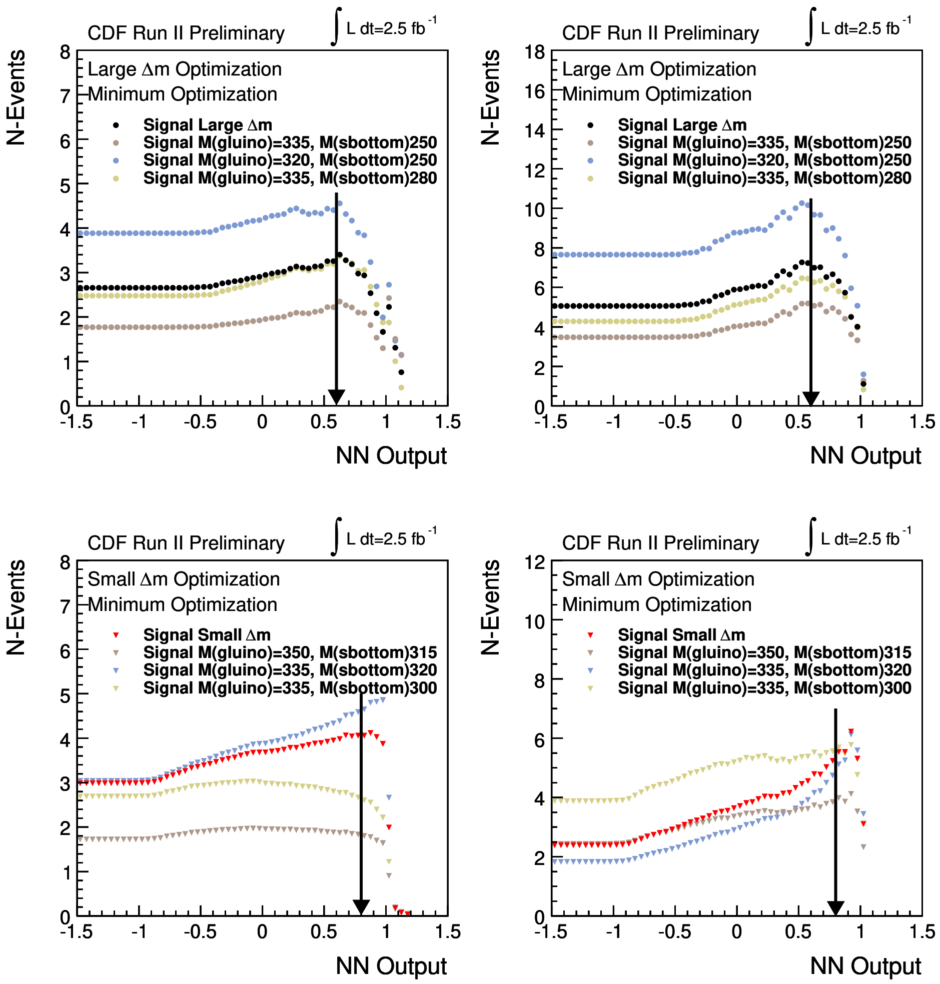

Figure 44: $S/sqrtB$ in the Top Neural Network's outputs for all optimizations. The arrow marks the applied cut. Other signal points surrounding the optimization one are shown

9 Systematic Uncertainties

A thorough study of systematic uncertainties on the estimation of background and signal expected events have been performed.

9.1 Background Uncertainties

For the prediction of the number of estimated backgrounds events, the following uncertainties are considered:

- **Jet Energy Scale (JES)**: A systematic error in the calorimeter energy scale affects the total transverse energy on the jets. $\pm 1\sigma$ variations in the jet energy corrections are computed in order to estimate the uncertainty on the jet energy scale. The corresponding shift in the $\not{E}_T$ was also included.
- **b-tagging Scale Factor (SF)**: The Monte Carlo simulation has an efficiency for tagging 5% larger than in data. In order to take in account the uncertainty due to this difference in efficiency $\pm 1\sigma$ variations in the scale factor were applied.
- **Mistag Rate**: The systematic error assigned to the tag rate matrix [11] is 4.8% in estimating the negative tags with the tight b-tagger. This uncertainty is already taken into account the Mistag rate error. The $\alpha\beta$ correction depends on the E_T of the jet and it is already applied to the Tag Rate matrix when using the Mistag Rate prediction. The absolute error assigned to the rate of each jets requested from the Matrix contains the previous error, the uncertainty in measuring the $\alpha\beta$ correction, and the statistical error in the matrix element.
- **Luminosity**: The systematic uncertainty in the luminosity is taken to be 6%.
- **ISR/FSR**: The uncertainty associated with the initial and final state radiation was evaluated by generating sample with more/less ISR/FSR according to the Joint Physics recommendation.
- **PDF**: The PDF uncertainty has been determined using the method described in reference [12]. In earlier analysis [1], it has been determined that a 2% uncertainty on the acceptance due to the choice of the PDF is sufficient.
- **QCD Multijet Background**:Since the method [10] we are using have not been thoroughly checked and it is not clear how the prediction may behave in the optimized regions (which are small corners of the phase space), we assign a conservative 50% uncertainty in the prediction.

  We assume any other uncertainty related to the estimation of the QCD multijet background will be covered by this, except those due to the substraction of the non-QCD contribution to the taggable sample in the optimized regions.
- **Top-Pair Production cross section**: We quote the uncertainty in the CDF measured value (11%) of the top-pair production cross section.

  This uncertainty is correctly propagated in the substraction from this sample to the Mistags. Correlations due to this are also taken into account.

- **Single Top Production cross section**: We quote the theoretical uncertainty in the single-top cross section (13%), as referenced by the CDF Single-Top Group [13].

  As with the Top-Pair production uncertainty, we have correctly propagated that associated to the Single-Top process into the corresponding substractions in the taggable samples.

- **Diboson Production cross section**: We quote the theoretical uncertainty in the WW and WZ cross section as 10% since the theoretical uncertainty in the ZZ is quoted as 20%.

  This uncertainty is correctly propagated in the substraction from this sample to the Mistags. Correlations due to this are also taken into account.

- **EWK Boson Production cross section**:Although the cross section for Z and W production are known to a high precision, we are using the inclusive processes in Pythia to perform estimations of $Z/W+$multijet processes. Because of this, we estimate a 40% uncertainty in the predictions [14]. In addition, this uncertainty is considered 100% correlated for all the Boson-production processes.

  This would be a safe overestimation of the uncertainty in a very suppressed background in the final selections.

  As with the Top-Pair production uncertainty, we have correctly propagated that associated to the Boson-Production processes into the corresponding substractions in the taggable samples.

- **Top mass in the Top pair NN's**: We include a systematic uncertainty in the final selections due to the Top pair NN's outputs variation as a function of the top quark mass used for the prediction. Details are shown in Appendix A later on this note.

9.2 Signal Uncertainties

The following systematic uncertainties: JES, b-tagging SF, Mistag Rate, Luminosity, ISR/FSR and PDF have been evaluated for the SUSY signal points. Where the same definitions as in the previous subsection are applicable here. In addiction a theoretical uncertainty in the gluino cross section of the 30% it was computed for the signal points.

Table 6, Table 7, Table 8 and Table 9 show the diferent contributions described in the present chapter for the four particular optimization regions.

PA Optimization 1 Exclusive Tag

Large Δm	BOSONS	DIBOSONS	Top Pair	Single Top	QCD	MISTAGS	**TOTAL**	SIGNAL
Central	1.85	0.56	7.13	0.077	0.92	5.65	**16.20**	13.68
JES	17.6%	13.7%	29.3%	38.5%	-	-4.3%	**17.8%**	9.2%
SF +1	4.6%	3.9%	2.4%	1.3%	-	-0.31%	**1.9%**	2.9%
SF -1	4.7%	4.0%	2.7%	1.7%	-	-0.31%	**2.0%**	2.6%
LUMI +1	6%	6%	6%	6%	-	-3.0%	**4.6%**	6%
xsec BOSONS	40%	-	-	-	-	-0.86%	**4.3%**	-
xsec DIBOSONS	-	11.4%	-	-	-	-0.001%	**0.36%**	-
xsec Top	-	-	11%	-	-	-0.86%	**5.4%**	-
xsec Sing.Top	-	-	-	13%	-	-0.016%	**0.056%**	-
QCD	-	-	-	-	50%	-	**2.8%**	-
MISTAGS +1	-	-	-	-	-	20.0%	**7.0%**	
MISTAGS -1	-	-	-	-	-	18.1%	**6.3%**	
TRIGGER +1	0%	0.002%	0.003%	0%	-	-0.0007%	**0.001%**	0.0005%
TRIGGER -1	0%	0.002%	0.003%	0%	-	-0.0007%	**0.001%**	0.0005%
PDF	2%	2%	2%	2%	-	-	**0.9%**	2%
ISR +1	10%	10%	10%	5.4%	-	-	**4.6%**	7.6%
ISR -1	10%	10%	10%	9.9%	-	-	**4.7%**	3.1%
FSR +1	5%	5%	5%	4.2%	-	-	**2.3%**	1.6%
FSR -1	5%	5%	5%	3.9%	-	-	**2.3%**	1.2%
xsec Gluino	-	-	-	-	-	-	-	30%
Top mass NN	-	-	15%	-	-	-	**7%**	-
TOTAL	45.8%	22.3%	37.7%	42%	50%	20.7%	**22.9%**	33.1%

Table 6: Backgrounds and signal systematic uncertainties for PA optimization 1 exclusivesive tags.

PB Optimization 1 Exclusive Tag

Small Δm	BOSONS	DIBOSONS	Top Pair	Single Top	QCD	MISTAGS	**TOTAL**	SIGNAL
Central	7.19	1.34	4.44	0.37	9.18	19.64	**42.15**	26.35
JES	9.4%	16.3%	16.9%	19.6%	-	-1.2%	**4.1%**	3.8%
SF +1	4.6%	4.3%	3.8%	3.9%	-	-0.057%	**1.4%**	1.8%
SF -1	4.7%	4.4%	3.9%	4.1%	-	-0.057%	**1.4%**	2.2%
LUMI +1	6%	6%	6%	6%	-	-0.19%	**2.0%**	6%
xsec BOSONS	40%	-	-	-	-	-1.9%	**5.9%**	-
xsec DIBOSONS	-	13.3%	-	-	-	-0.003%	**0.37%**	-
xsec Top	-	-	11%	-	-	-0.21%	**1.3%**	-
xsec Sing.Top	-	-	-	13%	-	-0.016%	**0.11%**	-
QCD	-	-	-	-	50%	-	**10.9%**	-
MISTAGS +1	-	-	-	-	-	41.4%	**19.3%**	-
MISTAGS -1	-	-	-	-	-	22.4%	**10.4%**	-
TRIGGER +1	0%	0.001%	0.01%	0.04%	-	-0.0003%	**0.001%**	0.005%
TRIGGER -1	0%	0.001%	0.01%	0.04%	-	-0.0003%	**0.001%**	0.005%
PDF	2%	2%	2%	2%	-	-	**1%**	2%
ISR +1	5%	5%	5%	3.2%	-	-	**2.4%**	4%
ISR -1	5%	5%	5%	2.1%	-	-	**2.4%**	2.6%
FSR +1	10%	10%	10%	5.4%	-	-	**4.9%**	1.7%
FSR -1	10%	10%	10%	3.3%	-	-	**4.8%**	1.2%
xsec Gluino	-	-	-	-	-	-	-	30%
Top mass NN	-	-	3%	-	-	-	**0.3%**	-
TOTAL	43.3%	25.0%	25.4%	24.5%	50%	41.5%	**24.1%**	31.3%

Table 7: Backgrounds and signal systematic uncertainties for PB optimization 1 exclusive tags.

PA Optimization 2 Inclusive Tags

Large Δm	BOSONS	DIBOSONS	Top Pair	Single Top	QCD	MISTAGS	**TOTAL**	SIGNAL
Central	0.11	0.07	1.91	0.027	1.48	0.94	**4.53**	14.88
JES	16.7%	10.3%	31.3%	14.0%	-	-8.6%	**17.0%**	9.6%
SF +1	10.8%	10.4%	10.2%	10.8%	-	-0.9%	**4.6%**	7.3%
SF -1	10.2%	9.9%	9.8%	10.2%	-	-0.9%	**4.4%**	7.4%
LUMI +1	6%	6%	6%	6%	-	-1.1%	**2.6%**	6%
xsec BOSONS	40%	-	-	-	-	-0.3%	**0.9%**	-
xsec DIBOSONS	-	12.5%	-	-	-	-12.5%	**0.2%**	-
xsec Top	-	-	11%	-	-	-2.1%	**5.0%**	-
xsec Sing.Top	-	-	-	13%	-	-0.03%	**0.1%**	-
QCD	-	-	-	-	50%	-	**16.3%**	-
MISTAGS +1	-	-	-	-	-	32.4%	**6.7%**	-
MISTAGS -1	-	-	-	-	-	27.0%	**5.6%**	-
TRIGGER +1	0%	0%	0.005%	0%	-	-0.0006%	**0.002%**	0.0003%
TRIGGER -1	0%	0%	0.005%	0%	-	-0.0006%	**0.0006%**	0.0004%
PDF	2%	2%	2%	2%	-	-	**0.9%**	2%
ISR +1	10%	10%	10%	5.4%	-	-	**4.6%**	7.6%
ISR -1	10%	10%	10%	9.9%	-	-	**4.7%**	3.1%
FSR +1	5%	5%	5%	4.2%	-	-	**2.3%**	1.6%
FSR -1	5%	5%	5%	3.9%	-	-	**2.3%**	1.2%
xsec Gluino	-	-	-	-	-	-	-	30%
Top mass NN	-	-	40%	-	-	-	**17%**	-
TOTAL	46.1%	23.1%	54.9%	24.3%	50%	35.9%	**31.1%**	33.9%

Table 8: Backgrounds and signal systematic uncertainties for PA optimization 2 inclusive tags.

PB Optimization 2 Inclusive Tags

Small Δm	BOSONS	DIBOSONS	Top Pair	Single Top	QCD	MISTAGS	**TOTAL**	SIGNAL
Central	0.39	0.12	0.61	0.045	0.60	0.58	**2.35**	8.49
JES	60.7%	11.7%	24.7%	13.0%	-	-4.8%	**25.5%**	7.4%
SF +1	10.8%	10.8%	10.5%	10.8%	-	-0.9%	**5.1%**	10.2%
SF -1	10.2%	10.2%	10.0%	10.2%	-	-0.9%	**4.8%**	9.7%
LUMI +1	6%	6%	6%	6%	-	-1.1%	**2.7%**	6%
xsec BOSONS	40%	-	-	-	-	-2.2%	**6.1%**	-
xsec DIBOSONS	-	20%	-	-	-	-0.003%	**0.9%**	-
xsec Top	-	-	11%	-	-	-1.3%	**3.1%**	-
xsec Sing.Top	-	-	-	13%	-	-0.09%	**0.2%**	-
QCD	-	-	-	-	50%	-	**12.8%**	-
MISTAGS +1	-	-	-	-	-	18.8%	**4.6%**	-
MISTAGS -1	-	-	-	-	-	19.6%	**4.8%**	-
TRIGGER +1	0%	0.002%	0.04%	2e-05%	-	-0.003%	**0.01%**	0.006%
TRIGGER -1	0%	0.002%	0.04%	2e-05%	-	-0.003%	**0.01%**	0.006%
PDF	2%	2%	2%	2%	-	-	**1%**	2%
ISR +1	5%	5%	5%	3.2%	-	-	**2.4%**	4%
ISR -1	5%	5%	5%	2.1%	-	-	**2.4%**	2.6%
FSR +1	10%	10%	10%	5.4%	-	-	**4.9%**	1.7%
FSR -1	10%	10%	10%	3.3%	-	-	**4.8%**	1.2%
xsec Gluino	-	-	-	-	-	-	-	30%
Top mass NN	-	-	57%	-	-	-	**15%**	-
TOTAL	74.6%	28.6%	65.6%	22.0%	50%	20.4%	**34.2%**	33.4%

Table 9: Backgrounds and signal systematic uncertainties for PB optimization 2 inclusive tags.

10 Results

10.1 Signal Regions Results

Four different signal regions were optimized for the present analysis. In this four regions the number of observed events events are in good agreement with the expected events from the SM processes as it is shown in Table 10 and Table 11.

CDF Run II Preliminary (1 Exclusive Tag)

Region	Large Δm Optimization	Small Δm Optimization
Boson production	1.8 ± 0.8	7.1 ± 3.1
Diboson production	0.6 ± 0.1	1.3 ± 0.3
Top pair production	7.1 ± 2.7	4.4 ± 1.1
Single top production	0.08 ± 0.03	0.4 ± 0.1
HF QCD Multijets	0.9 ± 0.5	9.2 ± 4.6
Light-flavour contamination	5.6 ± 1.2	19.6 ± 8.1
Total expected	16.2 ± 3.7	42.1 ± 10.1
Observed (2.5 fb^{-1})	18	29
Signal PA	13.7 ± 4.5	-
Signal PB	-	26.3 ± 8.2

Table 10: Table of predicted and observed events in the Large Δm and Small Δm signal regions with 1 exclusive tag.

CDF Run II Preliminary (2 Inclusive Tags)

Region	Large Δm Optimization	Small Δm Optimization
Boson production	0.1 ± 0.05	0.4 ± 0.3
Diboson production	0.07 ± 0.02	0.1 ± 0.03
Top pair production	1.9 ± 1.0	0.6 ± 0.4
Single top production	0.03 ± 0.01	0.04 ± 0.01
HF QCD Multijets	1.5 ± 0.7	0.6 ± 0.3
Light-flavour contamination	0.9 ± 0.3	0.6 ± 0.1
Total expected	4.5 ± 1.4	2.3 ± 0.8
Observed (2.5 fb^{-1})	5	2
Signal PA	14.9 ± 5.0	-
Signal PB	-	8.5 ± 2.8

Table 11: Table of predicted and observed events in the Large Δm and Small Δm signal regions with 2 inclusive tags.

Using the program Corrlim in order to extract the limits we have obtained that the presence of sbottom particles from gluino decays is excluded by detecting more than 8 events in the PA Signal Region 2 inclusive tags and more than 5.4 events in the PB Signal Region 2 inclusive tags. We have also obtained the exclusion limit for the 1 inclusive tag analysis founding that the presence of sbottom particles from gluino decays is excluded by detecting more than 16.2 events in the PA Signal Region 1 exclusive tag and more than 16.7 events in the PB Signal Region 1 exclusive tag.

In the following section 10.1.1 some kinematic distributions for each Sinal Region are shown (Fig 45, Fig 46, Fig 47 and Fig 48).

10.1.1 Signal Regions

Since the optimization process with Neural Networks reduced the amount of background in the final states to quantities almost negligible, the kinematic distributions itself in this final regions don't provide so much information. For this reason, in the following figures we will show the first jet E_T and $\not\!\!E_T$ as an example of background composition.

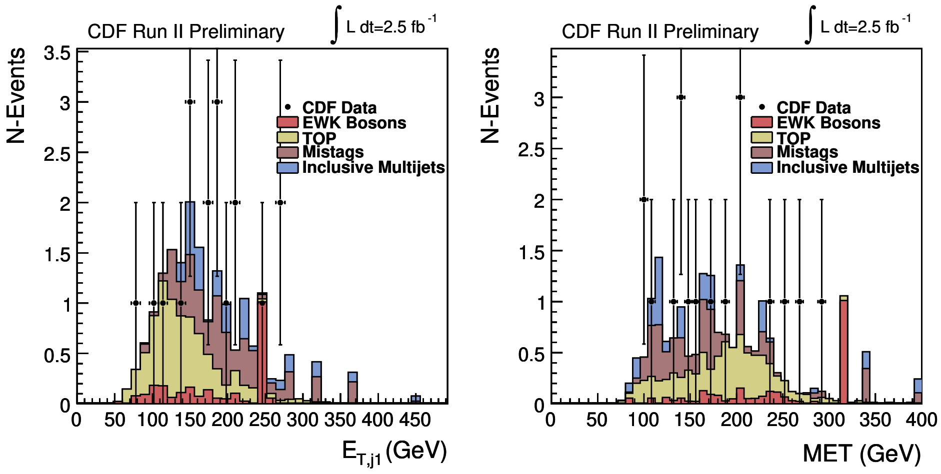

Figure 45: First jet E_T and $\not\!\!E_T$ distributions for the PA optimization 1 exclusive tag.

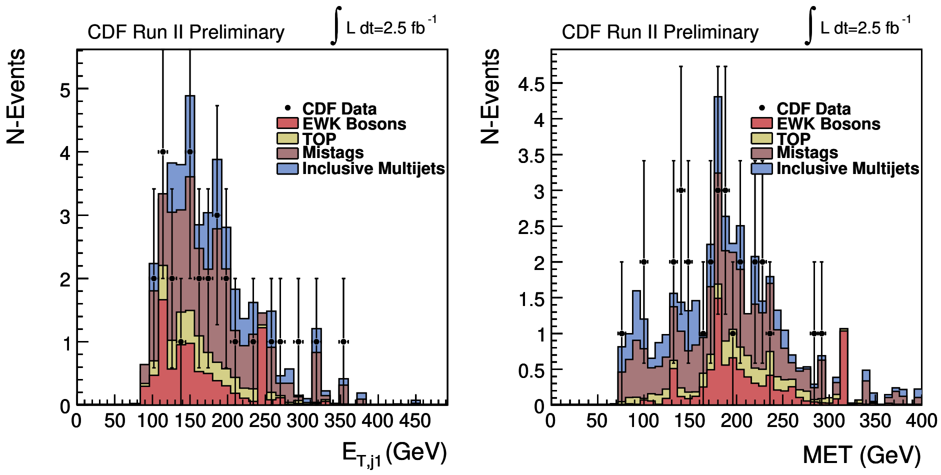

Figure 46: First jet E_T and $\not\!\!E_T$ distributions for the PB optimization 1 exclusive tag.

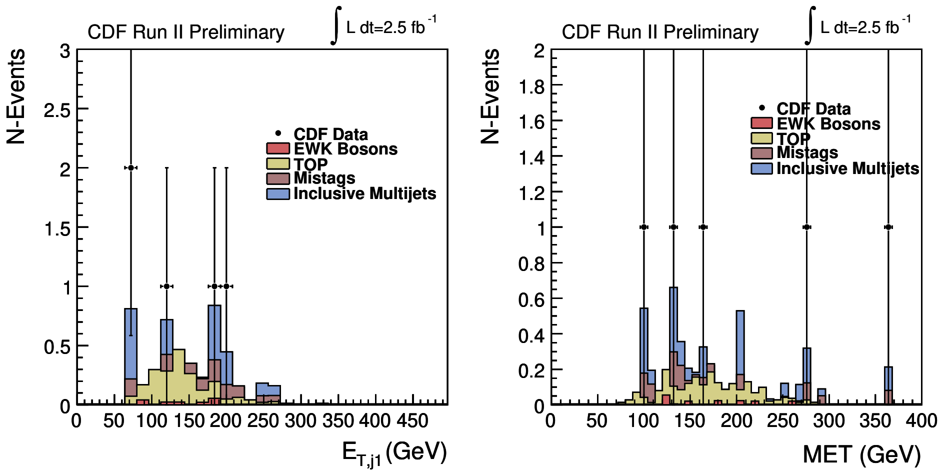

Figure 47: First jet E_T and $\not\!\!E_T$ distributions for the PA optimization 2 inclusive tags.

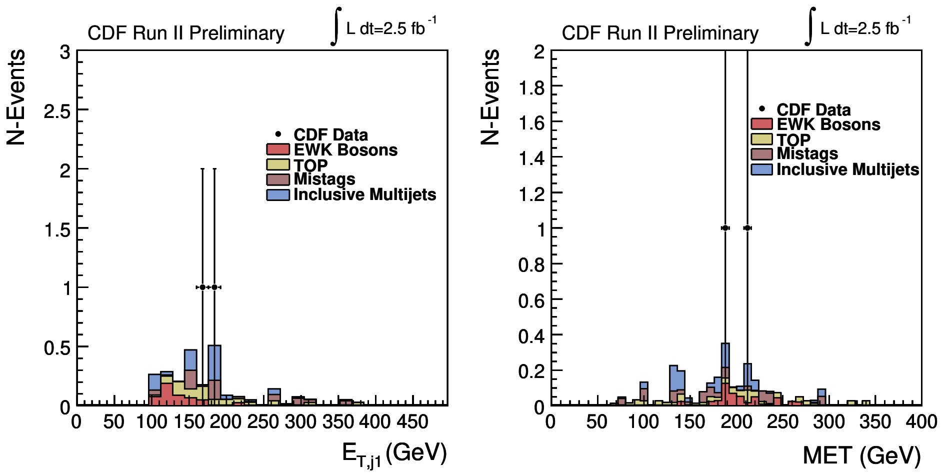

Figure 48: First jet E_T and $\not\!\!E_T$ distributions for the PB optimization 2 inclusive tags.

10.2 Observed Limit

This final section shows the observed limits obtained with 2.5 fb^{-1} of CDF data. In Figure 49 limits taking into account PA optimization only and PB optimization only are shown. Figure 50 show the the exclusion limit in terms of cross section with the points used for the calculations.

Figures 51 and 52 show the exclusion limit in terms of mass and cross section respectively.

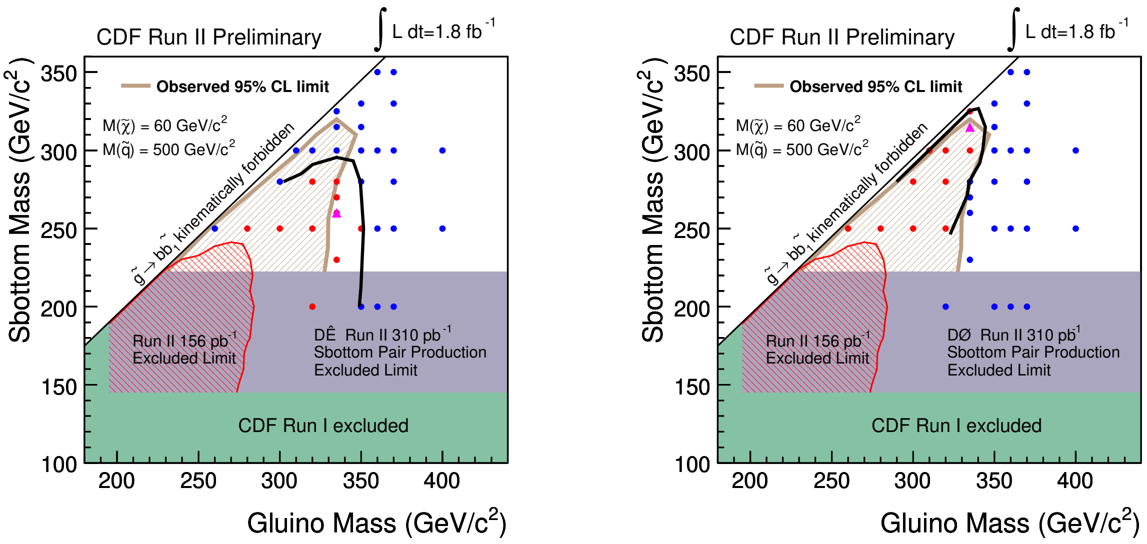

Figure 49: M($\tilde{b}$)-M($\tilde{g}$) exclusion plot at 95% C.L. assuming R-parity conservation. In brown, the limit from the previous version with 1.8 fb^{-1} and in black the lines from the PA optimization only (left) and PB optimization only (right).

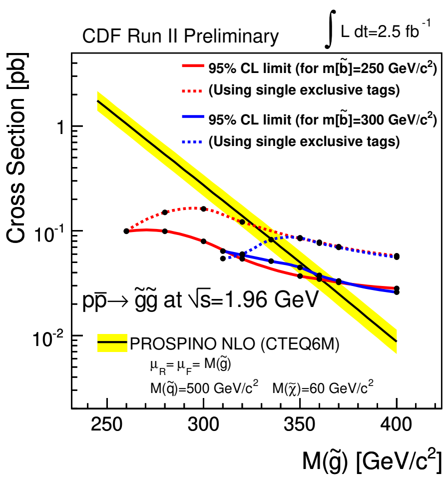

Figure 50: Observed limit in terms of cross section for two diferent masses of the sbottom (red and blue lines) in the 2 inclusive tags (solid lines) and 1 exclusive tag optimizations (dashed lines). Points used for the calculation are shown.

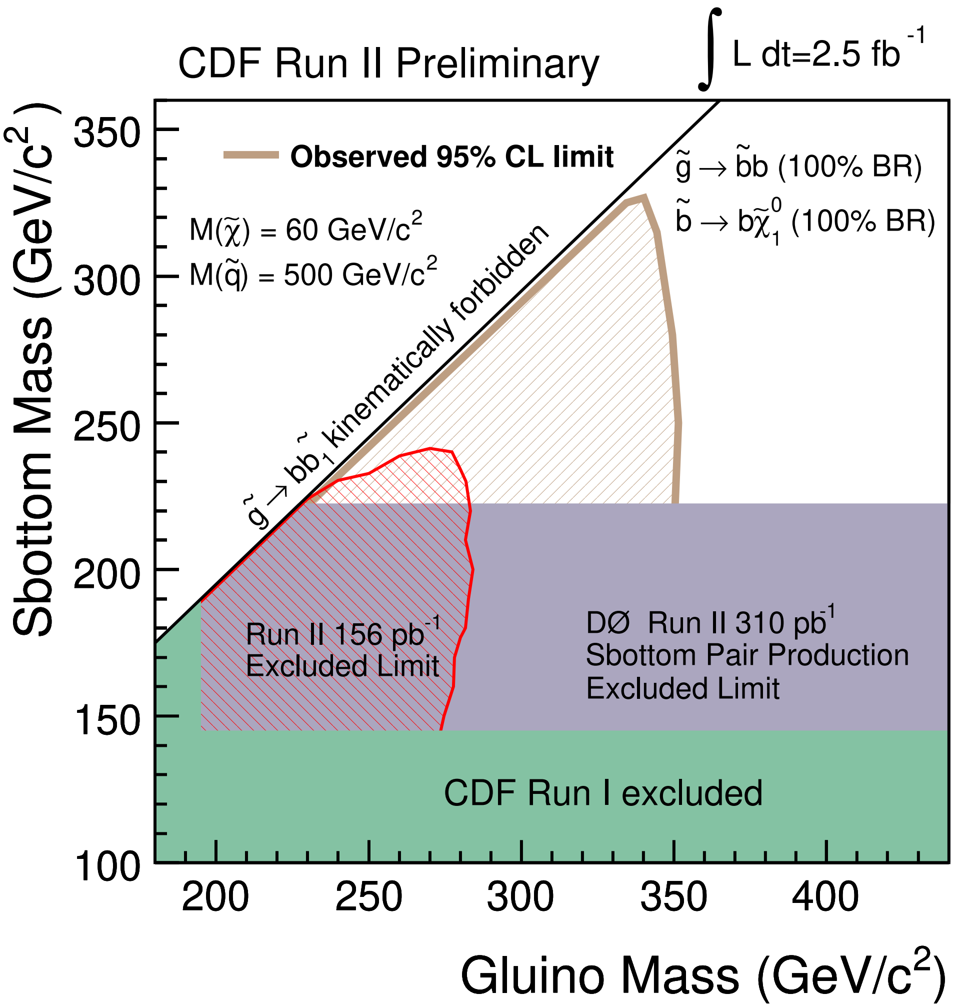

Figure 51: M($\tilde{b}$)-M($\tilde{g}$) exclusion plot at 95% C.L. assuming R-parity conservation.

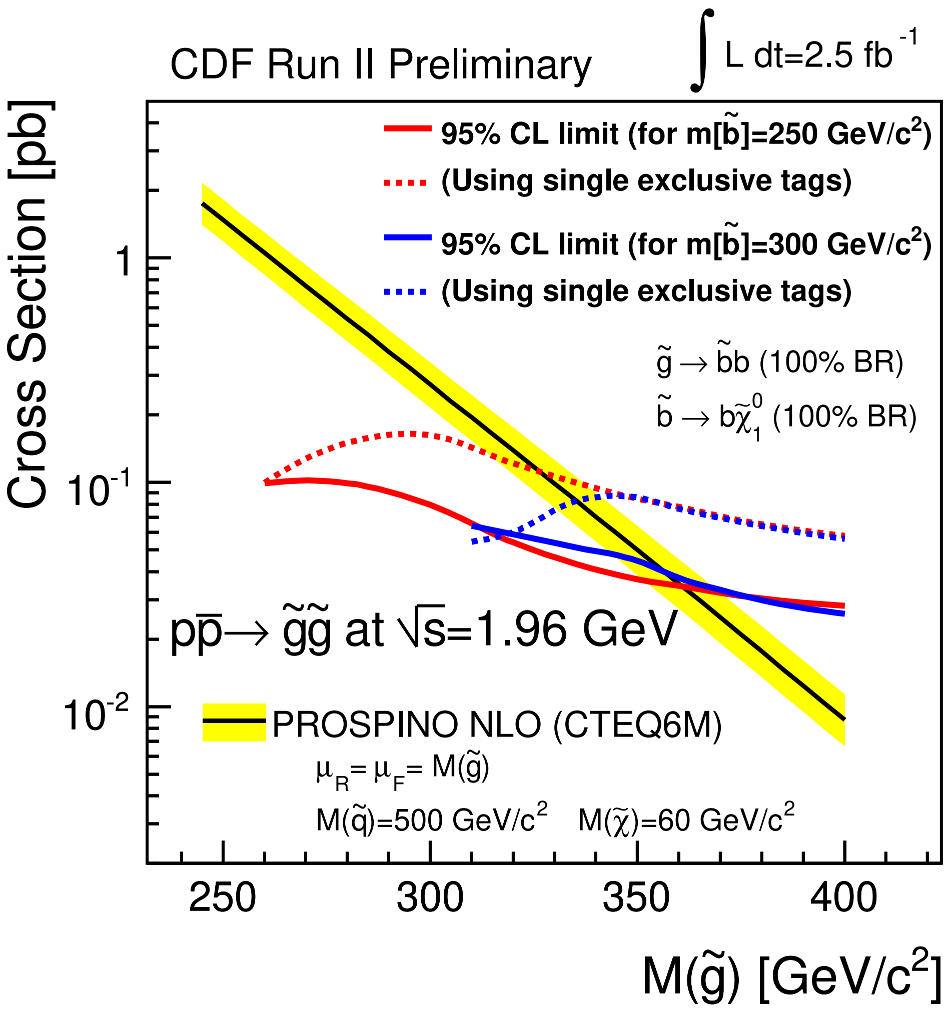

Figure 52: Observed limit in terms of cross section for two diferent masses of the sbottom (red and blue lines) in the 2 inclusive tags (solid lines) and 1 exclusive tag optimizations (dashed lines).

A Top pair NN dependence on the top quark mass

In the current analysis, the $t\bar{t}$ production background is estimated using MC with a top quark mass of 171.5 GeV/c^2. Since our signal optimization, described in Section 8, is based on a Neural Network trained with $t\bar{t}$ processes it is reasonable to check the top pair NN output dependence on the top quark mass.

To perform this check we use another $t\bar{t}$ MC sample with a top quark mass of 174.5 GeV/c^2 (test sample). In Figure 53 and Figure 54 we show the top pair NN output for the two different $t\bar{t}$ MC samples, in red the sample used in the analysis with its systematic uncertainty and test sample showed with dots.

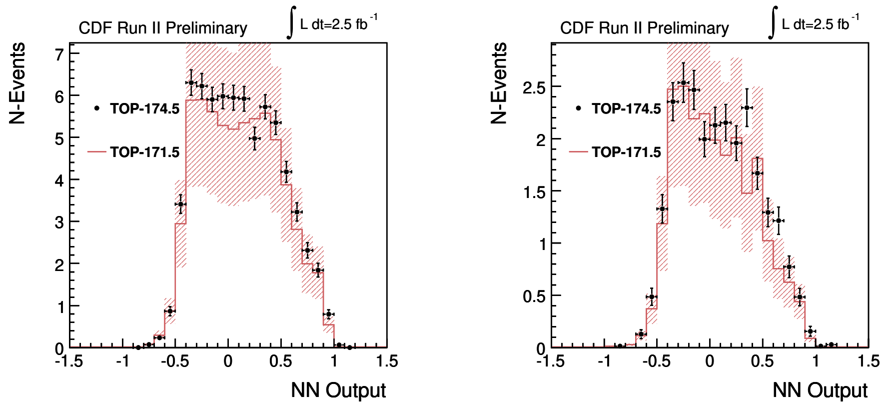

Figure 53: Top pair NN's output for the Large Δm optimization 1 exclusive tag (left) and Large Δm optimization 2 inclusive tags (right). Comparison between the sample used in the analysis (red line) and the test sample (dots)

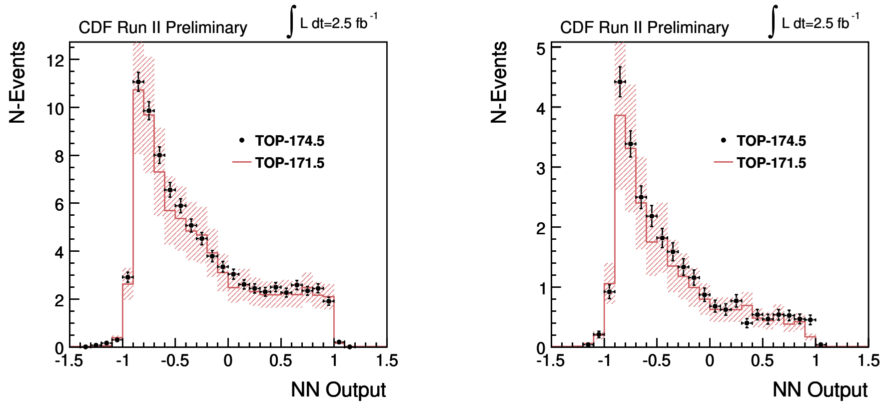

Figure 54: Top pair NN's output for the Small Δm optimization 1 exclusive tag (left) and Small Δm optimization 2 inclusive tags (right). Comparison between the sample used in the analysis (red line) and the test sample (dots)

From the difference observed between the two outputs in each region after the optimization cut we quote a systematic error already included in the calculations and showed in Section 9

B Dependences of the MUTARE prediction (2 inclusive tags) with the first or second tagged jet

As it is explained in Section 6 we are using the MUTARE Method [10] to estimate the QCD background in the double tag analysis using a matrix built over the 1-tag + 1-taggable sample. In this appendix we show the differences in the MUTARE prediction due to fact that the tagged jet is the first or the second jet. Since the matrix used for the prediction is built in the QCD Control Region where the second jet is aligned, by definition, with the $\not{E}_T$ we want to find out if there is any bias because of that.

For this study we use two MUTARE matrices, one of them built over the first jet tagged + 1-taggable sample and the other built over the second jet tagged + 1-taggable sample. Both matrices were built on the QCD region and are applied to the three control regions.

Figure 55 shows the QCD control region plots (2 inclusive tags) using the MUTARE prediction with the first jet tagged. By applying the QCD prediction to this region in wich was built we expect some disagreement due to the bias introduced for the fact that we are using a very espsecific subsample to built the matrix. However, the QCD prediction in the lepton and preoptimization control regions have good agreement using the first jet tagged matrix (Figure 56 and Figure 57).

Figure 58 shows the QCD control region plots (2 inclusive tags) using the MUTARE prediction with the second jet tagged. The same comments argued in the previous paragraph apply in this case. The QCD prediction in the lepton and preoptimization control regions have good agreement using the second jet tagged matrix (Figure 59 and Figure 60).

The differences observed by using the first jet tagged matrix or the second jet tagged matrix are not significant in the Lepton and Pre-optimization Control Regions and well covered by the 50% uncertatinty quoted in the analysis.

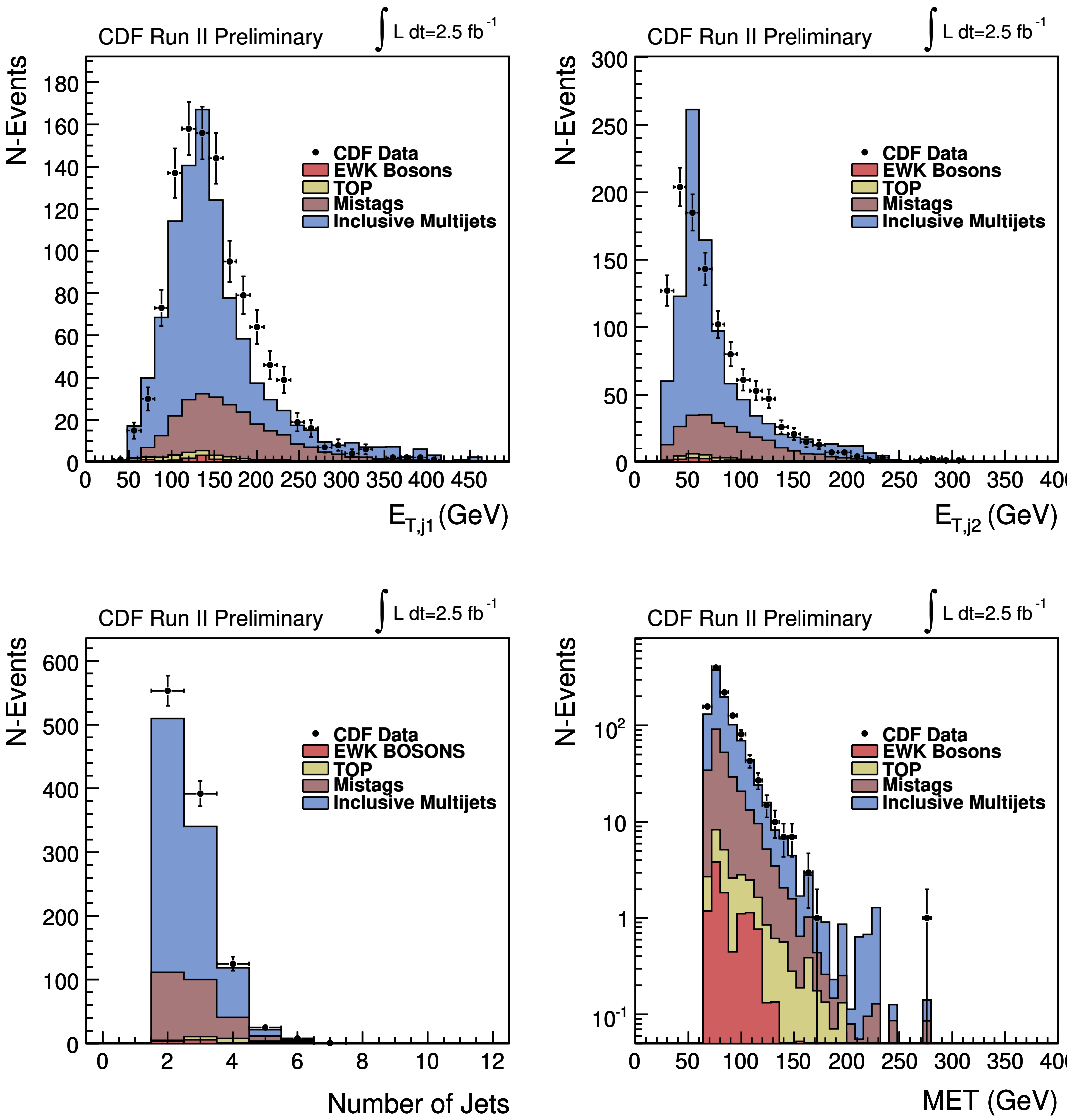

Figure 55: First jet E_T, second jet E_T, number of jets and $\not\!\!E_T$ in the QCD Control Region (2 inclusive tags), first jet tagged MUTARE matrix

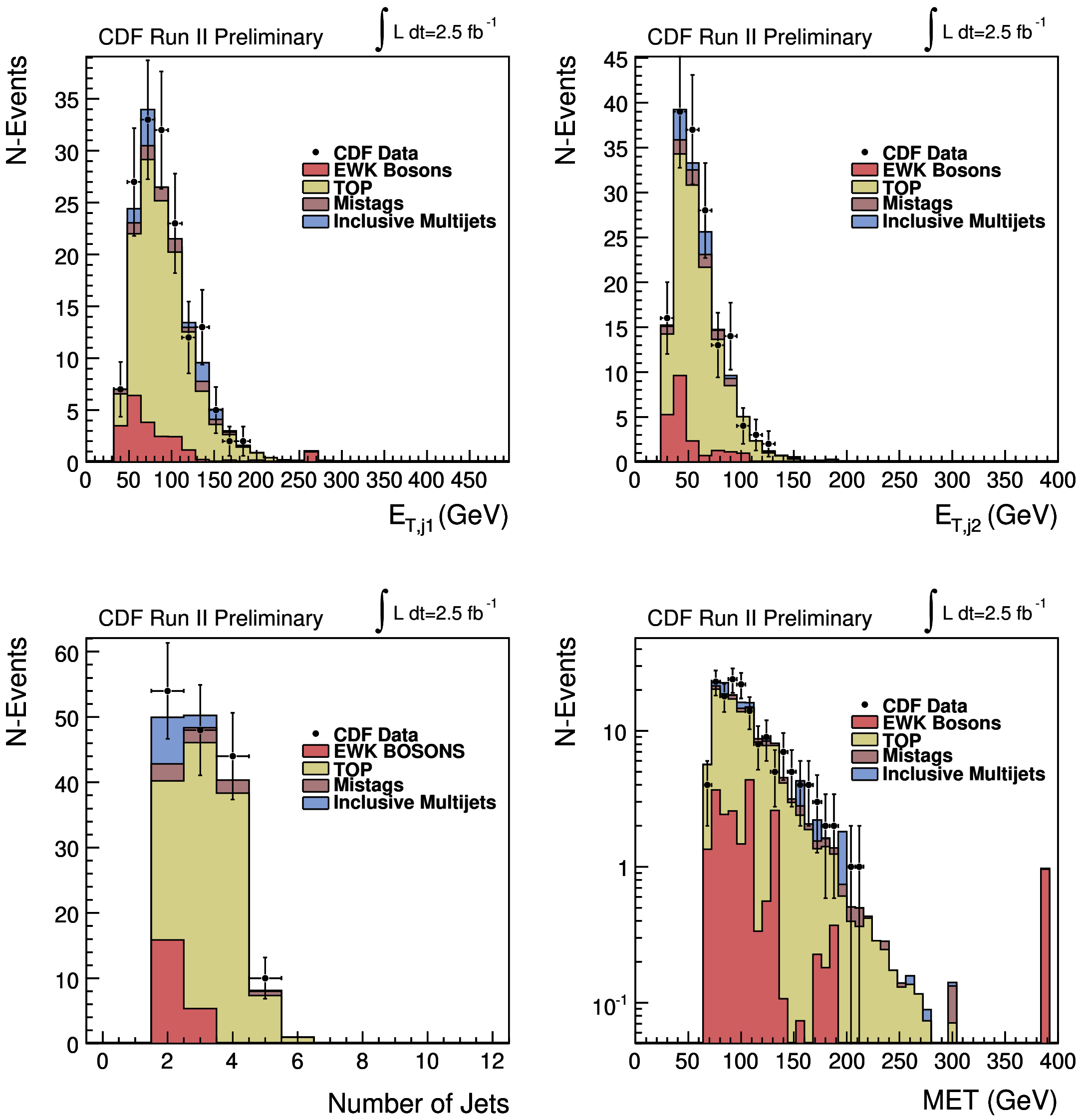

Figure 56: First jet E_T, second jet E_T, number of jets and $\not\!\!E_T$ in the Lepton Control Region (2 inclusive tags), first jet tagged MUTARE matrix

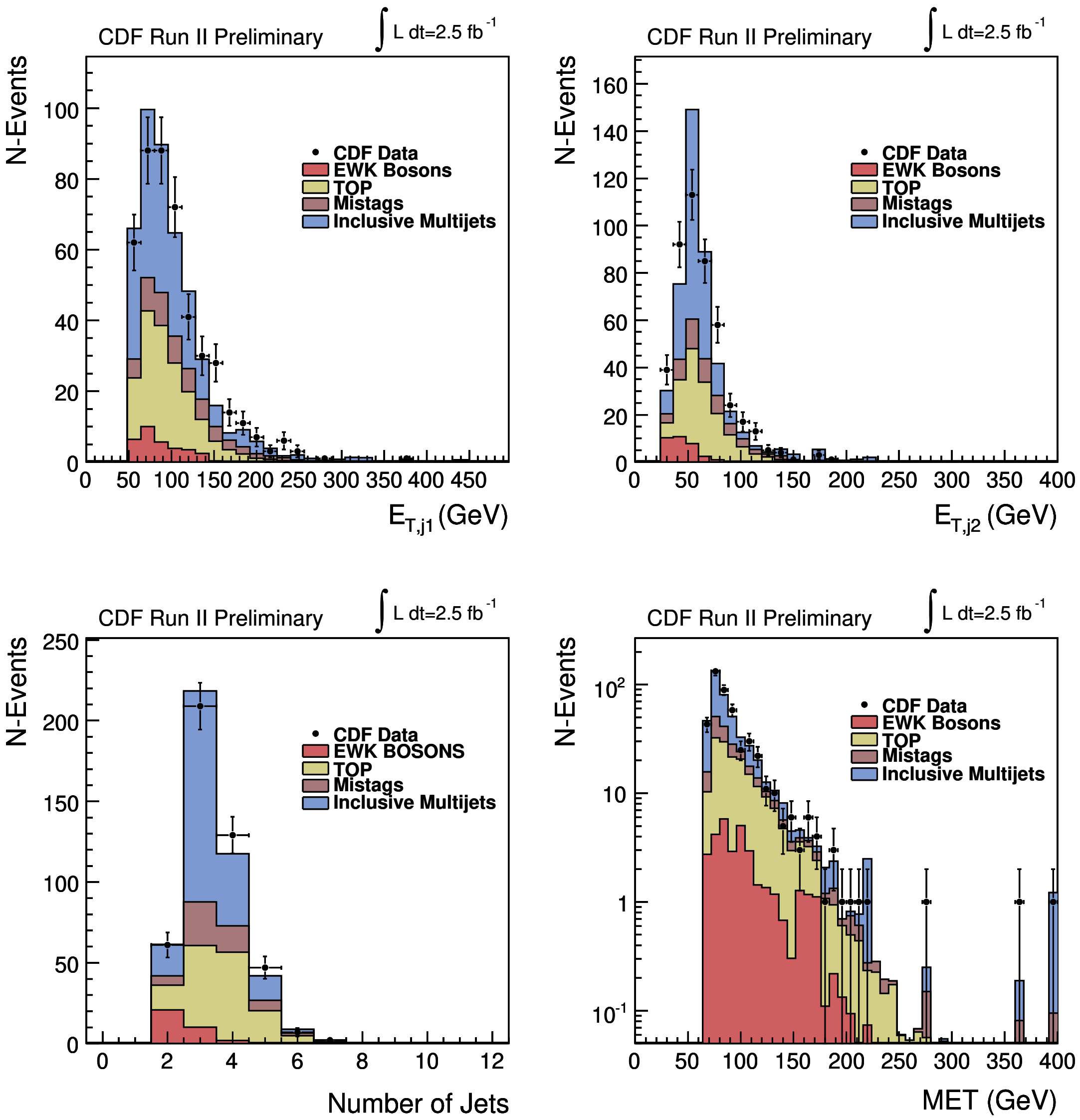

Figure 57: First jet E_T, second jet E_T, number of jets and $\not{E}_T$ in the Pre-Optimization Control Region (2 inclusive tags), first jet tagged MUTARE matrix

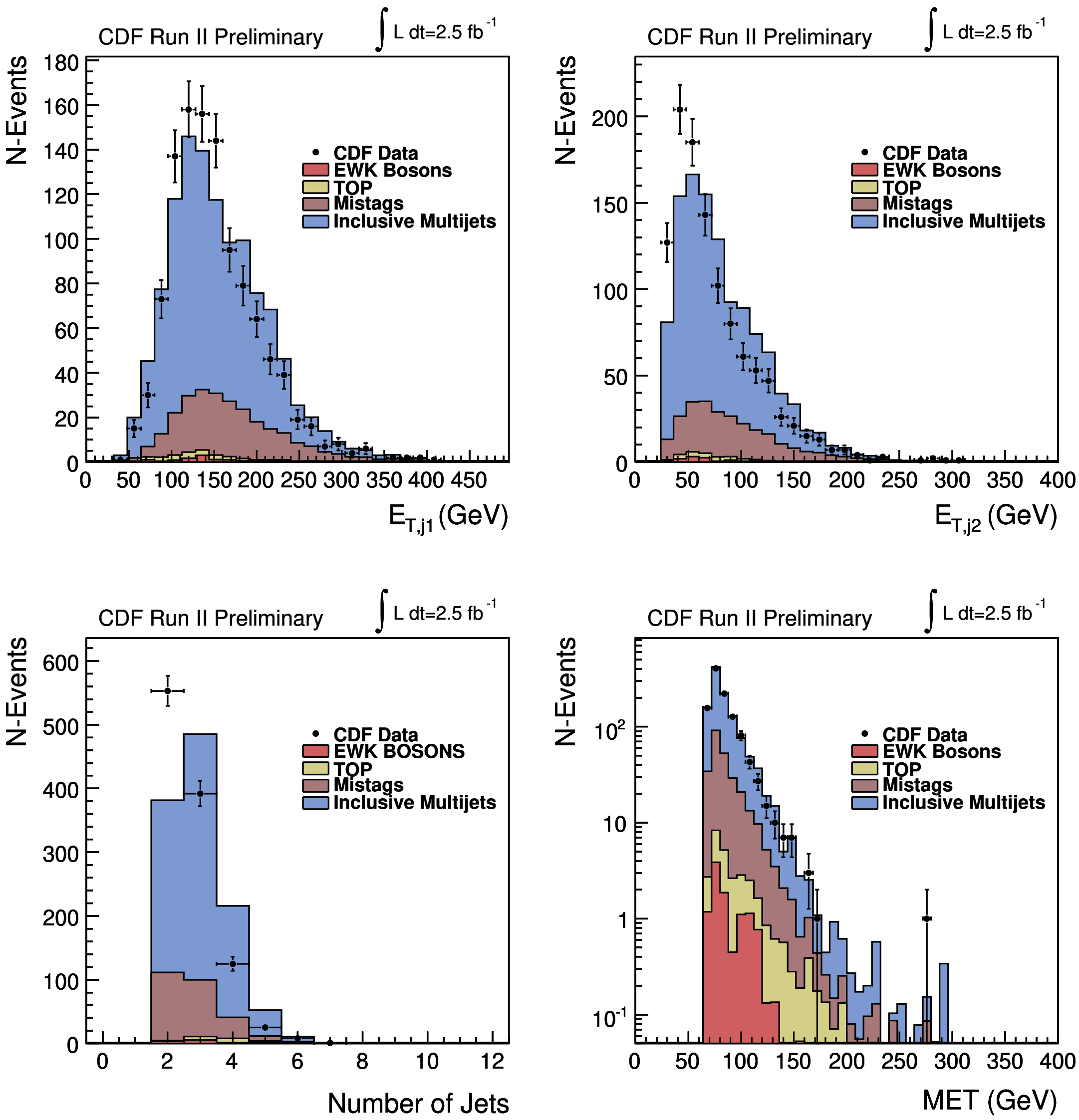

Figure 58: First jet E$_T$, second jet E$_T$, number of jets and $\not\!\!E_T$ in the QCD Control Region (2 inclusive tags), second jet tagged MUTARE matrix

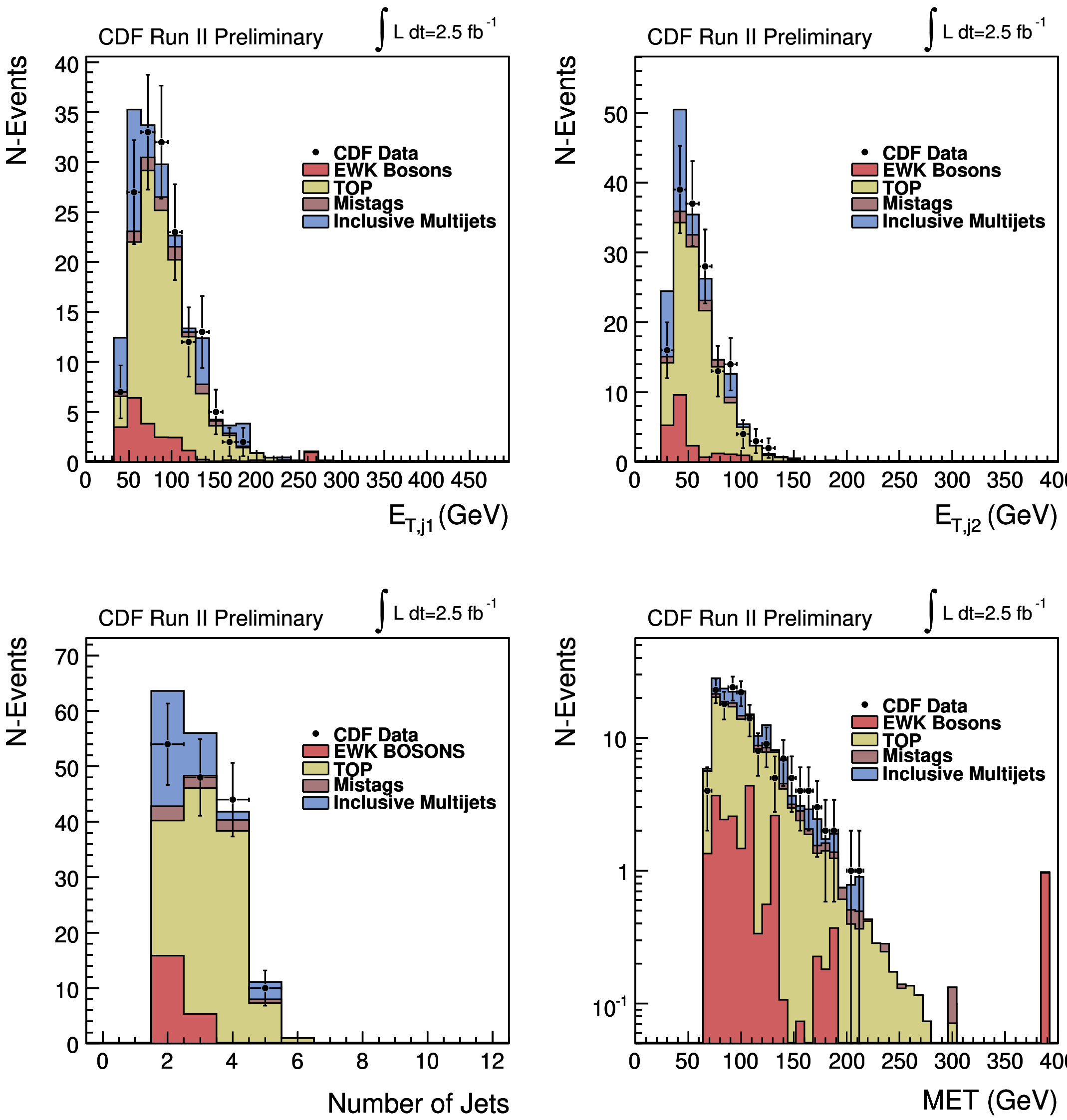

Figure 59: First jet E_T, second jet E_T, number of jets and $\not\!\!E_T$ in the Lepton Control Region (2 inclusive tags), second jet tagged MUTARE matrix

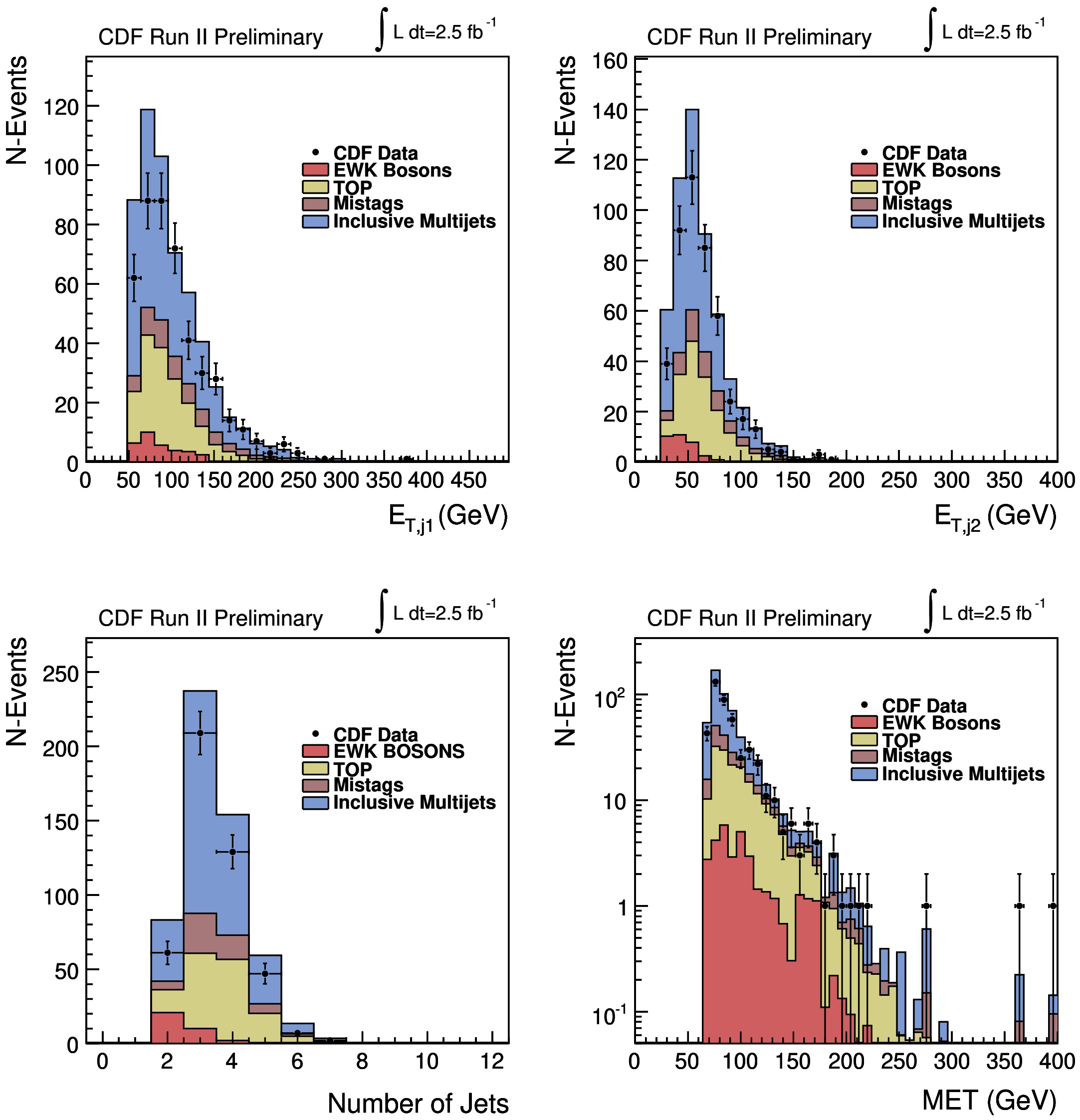

Figure 60: First jet E_T, second jet E_T, number of jets and $\not{E}_T$ in the Pre-Optimization Control Region (2 inclusive tags), second jet tagged MUTARE matrix

References

[1] C. Rott *et al.*, CDF Note CDF/ANAL/EXOTIC/CDFR/7025, 2004.

[2] M. Vidal *et al.*, CDF Note CDF/ANAL/EXOTIC/CDFR/9262, 2008.

[3] W. Beenakker, M. Hopker, M. Spira, and P. Zerwas, Nucl. Phys **B**, 51 (1997).

W. Beenakker, M. Hopker, and M. Spira, Prospino: A program for the production of supersymmetric particles in next-to-leading order qcd., hep-ph/9611232, 1996.

[4] T. Sjöstrand *et al.*, Comput. Phys. Commun. , 238 (2001).

[5] J. Pumplin *et al.*, New generation of parton distributions with uncertainties from global qcd analysis., JHEP 0207:012 (and hep-ph/0201195), 2002.

D. Stump *et al.*, Inclusive jet production, parton distributions, and the search for new physics., JHEP 0310:046,2003 (and hep-ph/0303013), 2003.

[6] M. D'Onofrio *et al.*, CDF Note CDF/ANAL/EXOTIC/PUBLIC/9174, 2008.

[7] O. González and M. Vidal, CDF Note CDF/ANAL/EXOTIC/CDFR/9231, 2008.

[8] D. Acosta *et al.*, CDF Note CDF/DOC/EXOTIC/CDFR/7410, 2004.

[9] The DØ Collaboration, Phys. Rev. Lett **97**, 171806 (2006).

[10] M. Vidal *et al.*, CDF Note CDF/PHYS/MISSING_ET/GROUP/9261, 2008.

[11] S. Budd *et al.*, CDF Note CDF/DOC/SEC_VTX/GROUP/8519, 2006.

[12] O. González and C. Rott, CDF Note CDF/PHYS/EXOTIC/CDFR/7051, 2004.

[13] B. Harris and other, Phys. Rev. **D66**, 054024 (2004).

Z. Sullivan and other, Phys. Rev. **D70**, 114012 (2004).

J. Campbell, K. Ellis, and F. Tramontano, Phys. Rev. **D70**, 094012 (2004).

N. Kidonakis, Phys. Rev. **D74**, 114012 (2006).

[14] V. Veszprémi *et al.*, CDF Note CDF/ANAL/EXOTIC/CDFR/8362, 2006.

A. Mehta and B. Heinemann, CDF Note CDF/ANAL/JET/CDFR/7780, 2005.

Acknowledgments

We thank John Conway and Tom Junk for their help and for providing us the code to extract the 95% CL exclusion. We thank also Carsten Rott for providing us the information about the previous work on this analysis. In addition we would like to thank the members of the Exotics and SUSY Working groups, and especially the conveners, for their support, comments and help during the development of the analysis.